ARTICLE

Properties of mine tailings for static liquefaction assessment

Jorge Macedo and Luis Vergaray

Abstract: Static liquefaction has been associated with numerous recent failures of tailings storage facilities (TSFs) around the world (e.g., the 2019 Brumadinho failure). These failures lead to devastating consequences for the environment and civil infrastructure as well as the loss of human lives. In this study, we present trends for the mechanical response of mine tailings considering (*i*) triaxial tests, (*ii*) bender element tests, and (*iii*) consolidation tests on 53 mine tailings materials (including recent case histories). These materials have a broad range of states, particle size distributions, and compressibility. The trends are evaluated in the context of static liquefaction using critical state soil mechanics concepts, focusing on the variation of the shear strength (residual and peak), state and brittleness soil indexes, excess pore pressure indexes, instability stress ratios, and dilatancy. In particular, we highlight that mine tailings' mechanical properties reflect both the properties of the particles themselves and the relative proportions of different particle sizes. For instance, the observed trends suggest that particle gradation influences the small strain stiffness and dilatancy; the proportion of voids to the size of fine particles influences strength, and particle shape affects dilatancy. Finally, we propose static liquefaction screening indexes based on the observed trends.

Key words: mine tailings, static liquefaction, mechanical properties.

Résumé : La liquéfaction statique a été associée à plusieurs défaillances récentes d'installations de stockage de résidus (TSF) dans le monde (par exemple, la défaillance de Brumadinho en 2019). Ces défaillances provoquent des conséquences dévastatrices pour l'environnement et les infrastructures civiles, ainsi que des pertes de vies humaines. Dans cette étude, nous présentons les tendances de la réponse mécanique des résidus miniers en considérant (*i*) des essais triaxiaux, (*ii*) des essais par éléments pliés et (*iii*) des essais de consolidation sur 53 matériaux de résidus miniers (y compris des cas récents). Ces matériaux présentent un large éventail d'états, de distributions granulométriques et de compressibilité. Les tendances sont évaluées dans le contexte de la liquéfaction statique en utilisant les concepts de la mécanique des sols à l'état critique, en se concentrant sur la variation de la résistance au cisaillement (résiduelle et maximale), les indices d'état et de fragilité des sols, les indices de surpression interstitielle, les rapports de contrainte d'instabilité et la dilatation. En particulier, nous soulignons que les propriétés mécaniques des résidus miniers reflètent à la fois les propriétés des particules elles-mêmes et les proportions relatives des différentes tailles de particules. Par exemple, les tendances observées suggèrent que la gradation des particules influence la rigidité à petite déformation et la dilatation; la proportion de vides par rapport à la taille des particules fines influence la résistance, et la forme des particules affecte la dilatation. Enfin, nous proposons des indices de dépistage de la liquéfaction statique basés sur les tendances observées. [Traduit par la Rédaction]

Mots-clés : résidus miniers, liquéfaction statique, propriétés mécaniques.

Introduction

The static liquefaction of mine tailings has caused numerous recent failures (e.g., the 1985 Stava disaster in Italy (Chandler and Tosatti 1995); the 1994 Merriespruit failure in South Africa (Fourie and Papageorgiou 2001); the 2014 Mount Polley disaster in Canada (Morgenstern et al. 2015); the 2015 Fundao failure in Brazil (Morgenstern et al. 2016); the 2018 Cadia failure in Australia (Morgenstern et al. 2019); and the 2019 Brumadinho failure in Brazil (Robertson et al. 2019)). Such failures of tailings storage facilities (TSFs) have caused unprecedented devastating consequences for the environment, infrastructure damage as well as human losses. For example, the Fundao failure is considered the largest environmental disaster in Brazil, and the Mount Polley failure in Canada is one of the worst disasters in modern Canadian history. These failures have triggered international debates regarding the safety of TSF systems. In particular, the conditions that result in static liquefaction of mine tailings

remain a considerable concern affecting the financial viability of mines and the willingness of governments to allow mining.

From a technical standpoint, it is worth highlighting that static liquefaction is just another facet of soil behavior under loading, and hence it should be explained under a mechanistic framework. A historical perspective on the definition of the liquefaction phenomena is provided in Jefferies and Been (2015), where the authors highlight the lessons after the Calaveras dam failure (Hazen 1918) and the definition of the critical void ratio concept (Casagrandre 1936) as part of the pioneering efforts to advance the understanding of liquefaction. In a historical context, one of the first attempts to account for static liquefaction at a design stage goes back to the work by the US Army Corps of Engineers (USACE), having designed and constructed Franklin Falls dam to resist static liquefaction ("sand flow failure" in the terminology of the time) approximately 80 years ago. This initial work by the USACE, documented in Lyman (1938), developed over the following years into the mechanistic framework now known as critical

J. Macedo and L. Vergaray. Georgia Institute of Technology, Atlanta, Ga., USA.

Corresponding author: Jorge Macedo (email: jorge.macedo@gatech.edu).

Fig. 1. Range of particle size distribution for the materials considered in this study. Materials 01 to 07 are made available as part of this study. Materials 08 to 53 were compiled from Fourie and Papageorgiou (2001), Shuttle and Cunning (2007), Carrera et al. (2011), Anderson and Eldridge (2011), Bedin et al. (2012), Schnaid et al. (2013), Been (2016), Li et al. (2018), Reid et al. (2018), Li and Coop (2019), Raposo (2016), Torres (2016), Morgenstern et al. (2016), Riemer et al. (2017), Li (2017), Robertson et al. (2019), Macedo and Petalas (2019), Gill (2019), Reid and Fanni (2020), and Reid et al. (2021). [Colour online.]
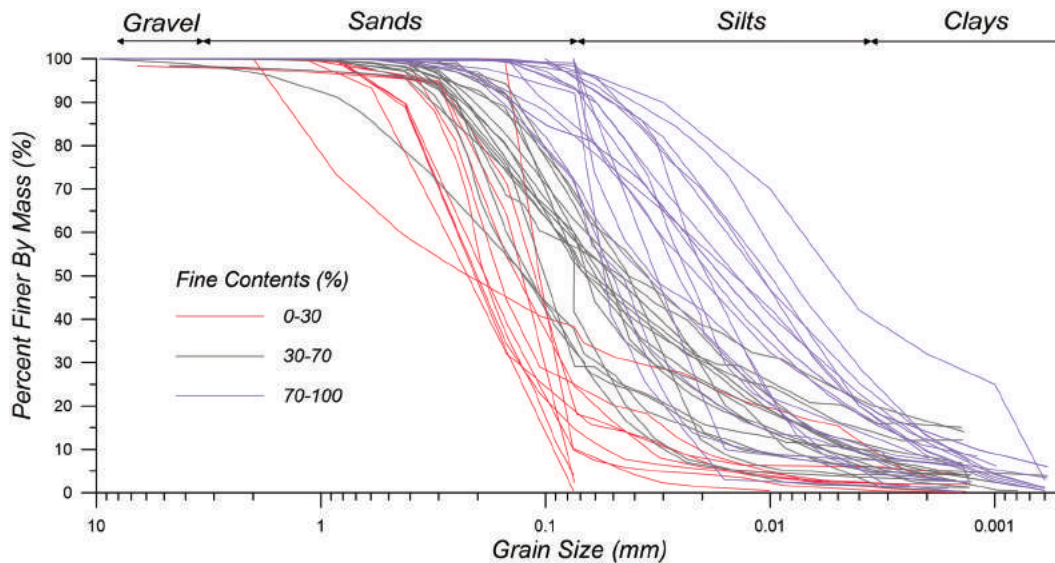
state soil mechanics (CSSM). Arguably, CSSM is now the preeminent methodology for understanding static liquefaction, having been used in the mining industry by the expert panels retained to investigate recent TSF failures such as, for example, Fundao (Morgenstern et al. 2016), Cadia (Morgenstern et al. 2019), and Brumadinho (Robertson et al. 2019).

In the US, approximately 1200 TSFs exist, with 60% of them having a significant hazard according to the USACE classification (USACE 2016). Hence, the safety of TSFs is an important issue. In some scenarios, the deposited tailings in a TSF are an essential component of the overall physical stability of a TSF. This is particularly the case for upstream and centerline dams, which may have a high associated risk, not only during their operation but also when they are considered inactive (e.g., the Brumadinho dam was inactive since 2015 and failed in 2019). In these scenarios, an adequate understanding of the mechanical response of tailing materials is essential for understanding the response of the overall TSF system. Moreover, as engineering practice is moving more towards finite element or finite difference-based stress analyses (e.g., the evaluations performed in the forensic studies after recent failures), understanding the mechanical response of mine tailings is also fundamental for the calibration of constitutive models that can later be used in numerical simulations. This is not simple because mine tailings are often characterized as intermediate materials (pure silts or sandy silts), which represents a fundamental challenge for understanding their mechanical response. Tailings are also geologically young materials, with angular grains rather than subrounded and often with lower proportions of quartz than many natural soils; thus, standard geotechnical correlations should not be taken as applicable to tailings without detailed consideration of these factors.

Previous efforts on understanding the trends in the mechanical response of particulate materials under monotonic loadings have been mainly focused on sands with low fine contents (e.g., Sadrekarimi 2014; Jefferies and Been 2015; Rabbi et al. 2019). For example, Sadrekarimi (2016) used results from laboratory tests under different boundary conditions (e.g., triaxial, plane strain) to find trends in the peak and residual normalized strengths of sand materials with respect to the brittleness index (Bishop 1971).

Rabbi et al. (2019) used experimental results from an Australian sand with 10% fine contents (FC) to present trends between a modified version of the brittleness index and different parameters that characterize the state of a soil material (e.g., the state parameter defined by Been and Jefferies 1985). In addition, Rabbi et al. (2019) also presented trends for the stress ratio ($\eta = q/p$, where q is the deviatoric stress, and p is the effective mean stress) at liquefaction triggering against different parameters that represent soil state.

In terms of mine tailings, the experimental studies that have evaluated their mechanical response and the associated mechanical parameters are somewhat limited compared to sand materials (e.g., Jefferies and Been 2015; Shuttle and Jefferies 2016; Fourie and Tshabalala 2005; Carrera et al. 2011). In terms of trends extracted from a large number of experimental tests, the authors are only aware of the study by Smith et al. (2019), who presented trends for the parameters that define a linear critical state line (i.e., the slope and altitude at low stresses), and the variation of the brittleness index and a normalized version of the state parameter. In a broader perspective, the mechanical properties in particulate materials (including mine tailings) reflect both the properties of the particles themselves and the relative proportions of the different particle sizes, which affect how easily particle movements create new contacts and the available space of particles to move into. Some previous research exploring particle shape and gradation effects on the macromechanical response of particulate materials include the work of Cho et al. (2006), who explored the role of particle properties on mechanical properties of uniformly graded clean sands. Torres-Cruz and Santamarina (2020) explored the trends of mine tailings critical state line (CSL) properties in terms of the minimum void ratio ($e_{\min}$), concluding that $e_{\min}$ could be used to characterize the variation of the CSL properties in the field. Payan et al. (2016) evaluated the effects of particle sizes on the stiffness of sands by considering the coefficient of uniformity (C_u), concluding that gradation has an important effect on the stiffness of sand materials.

In this study, we present trends for mechanical-based parameters that control the response of mine tailings, in the context of static liquefaction, which have not been previously explored

Fig. 2. Normalized stress–strain and stress path curves for material 1 (*a*, *b*), material 2 (*c*, *d*), and material 3 (*e*, *f*). Additional information for the tests in materials 1 to 7 is presented in the Table A2 of Appendix A. [Colour online.]
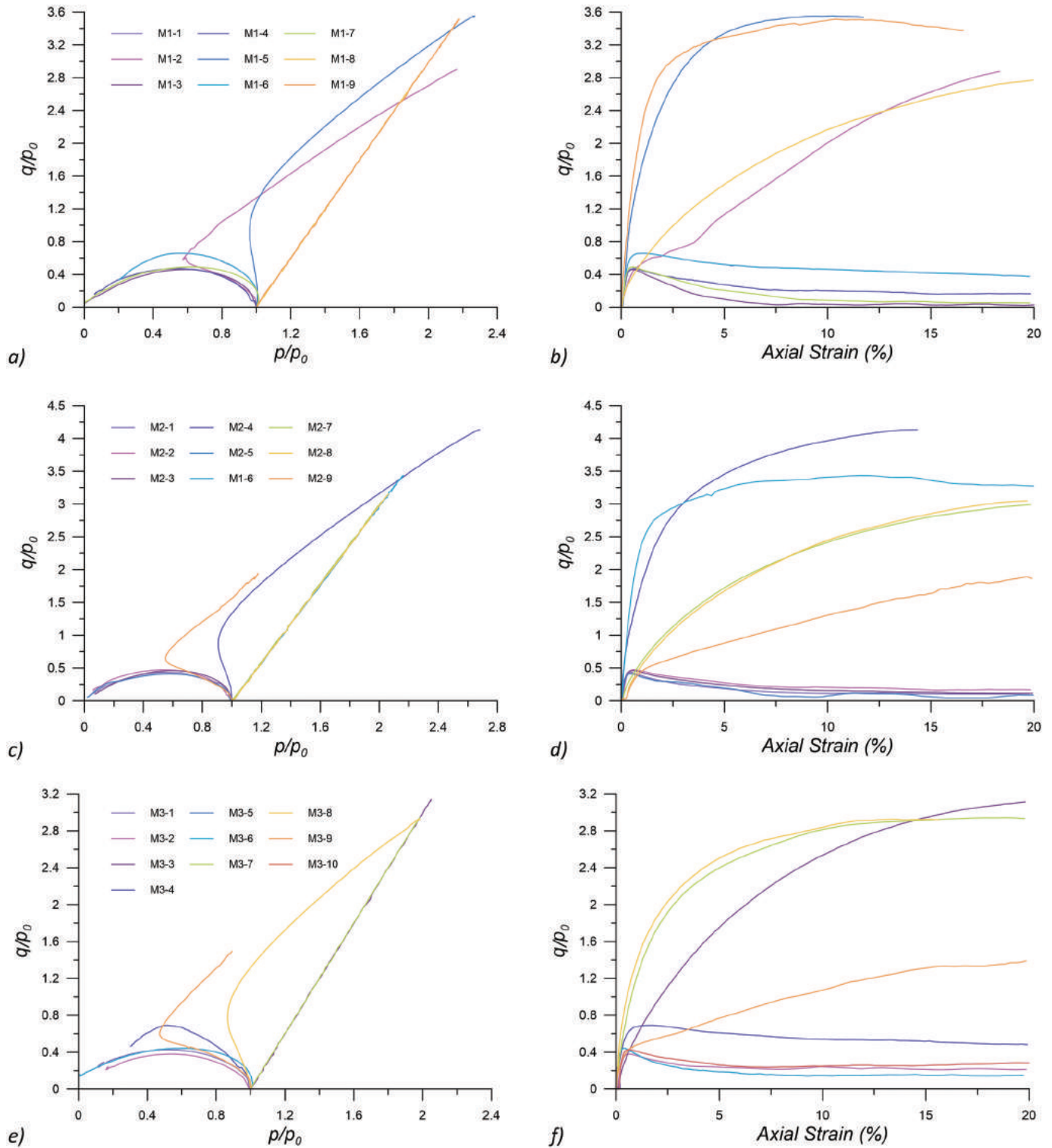
considering a large set of tailings materials. Another aspect that we highlight is the influence of the relative proportions of particle sizes on the macromechanical response of mine tailings. We consider a broad range of states, a range of particle size distributions (i.e., from silty sand to almost pure silt mine tailings), a broad range of compressibility, and a broad range of particle

gradations. The trends are presented using results from 53 mine tailings materials (including available data from the recent failures previously discussed), which have been processed in a uniform manner. In some instances, numerical simulations with the Norsand model (Jefferies 1993; Jefferies and Been 2015), referred to as Norsand in this study, are used to complement the

Fig. 3. Illustration of the estimation of mechanical-based parameters consistent with the critical state theory for material 12. (*a*) CSL estimation, (*b*) $\eta_{\max}$ versus $D_{\min}$ plot to estimate M_{tc} and N, (*c*) state-dilatancy relationship to estimate χ, and (*d*) G versus p plot to estimate A and B. [Colour online.]
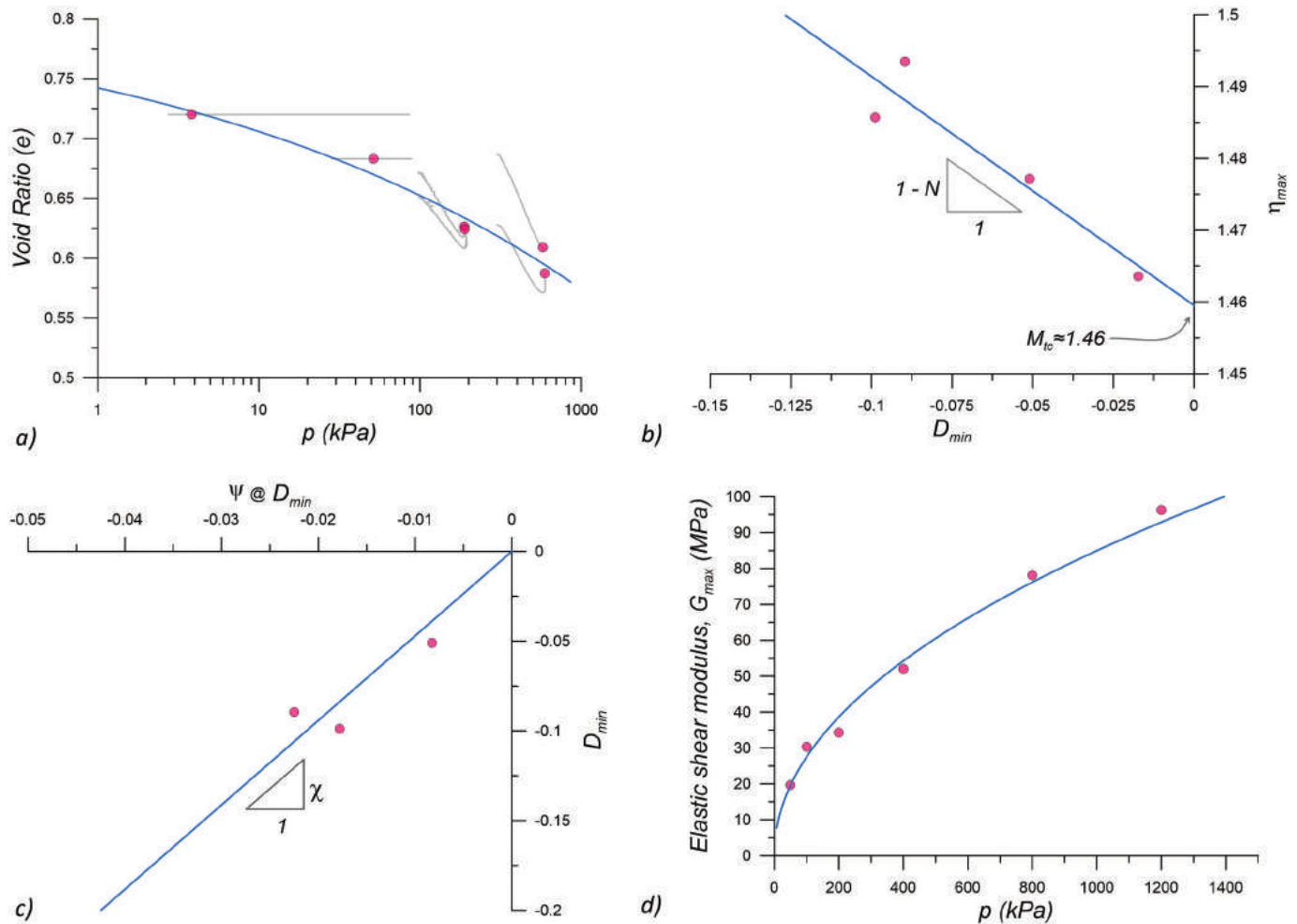
observations from experimental-based trends. Finally, we provide screening indexes for the assessment of static liquefaction in mine tailings using insights from the observed trends.

Materials database

Figure 1 shows the particle size distribution for the materials considered in this study, separating them by fine contents for easier visualization. The data for materials 01 to 07 are made available as part of this study, considering the following information: (*i*) triaxial compression drained (Tx-CD) and triaxial compression undrained (Tx-CU) tests, defining a CSL, (*ii*) consolidation (using a constant rate of strain procedure), and (*iii*) bender elements to evaluate the stiffness (i.e., shear modulus). Materials 08 to 53 were compiled from Shuttle and Cunning (2007), Anderson and Eldridge (2011), Bedin et al. (2012), Schnaid et al. (2013), Been (2016), Li et al. (2018), Li and Coop (2019), Raposo (2016), Torres (2016), Morgenstern et al. (2016), Riemer et al. (2017), Li (2017), Robertson et al. (2019), Macedo and Petalas (2019), Gill (2019), Reid and Fanni (2020), Reid et al. (2018), Macedo et al. (2020), Reid et al. (2021), Fourie and Papageorgiou (2001), and Carrera et al. (2011). In particular, material 22 corresponds to the Fundao failure, materials 24 to 27 correspond to the Cadia failure, materials 30 to 32 correspond to the Brumadinho failure, materials 46 to 49 correspond to the Merriespruit failure, and materials 50 to 53 correspond to the Stava failure. The database contains 334 triaxial tests, 49 consolidation tests, and

54 bender element tests. The mine tailings correspond to different ores (i.e., gold, iron, silver, copper, zinc, platinum), and they cover a broad range of fine contents (FC = 0%–100%), initial confining stress (20–6000 kPa), specific gravity (G_s = 2.63–4.89), and states (i.e., very loose to dense). Additional details are included in Table A1 of Appendix A.

In the case of the materials 01 to 07, a washed sieve analysis and specific gravity were completed on each specimen prior to testing. The specimens were then prepared using moist tamping, during which the specific gravities were used to calculate void ratios and dry densities before each test. Initial height and diameter measurements were taken before shearing, and void ratios were measured using the end-of-test soil freezing technique (Sladen and Handford 1987; Jefferies and Been 2015; Reid et al. 2021), which were used to estimate the void ratio change during the tests. The "under-compaction" method (Ladd 1978) was used to improve the uniformity of the prepared specimens by varying the weight of each compacted layer. A vacuum (<5 kPa) was applied to hold the specimens before they are placed in the triaxial cell (e.g., for saturation purposes). The moist tamping technique has been selected because it enhances specimen homogeneity, allows better control over the specimen's void ratio, and promotes strain-softening (Sadrekarimi and Riveros 2020; Al-Tarhouni et al. 2011; Chen and van Zyl 1988; Sladen et al. 1985; Fourie and Tshabalala 2005; Reid et al. 2018; Schnaid et al. 2013). Recently,

Fig. 4. Illustration of the adopted criteria to characterize different responses in undrained triaxial. Δu is the excess pore pressure, and σ'_0 is the initial vertical effective stress. [Colour online.]
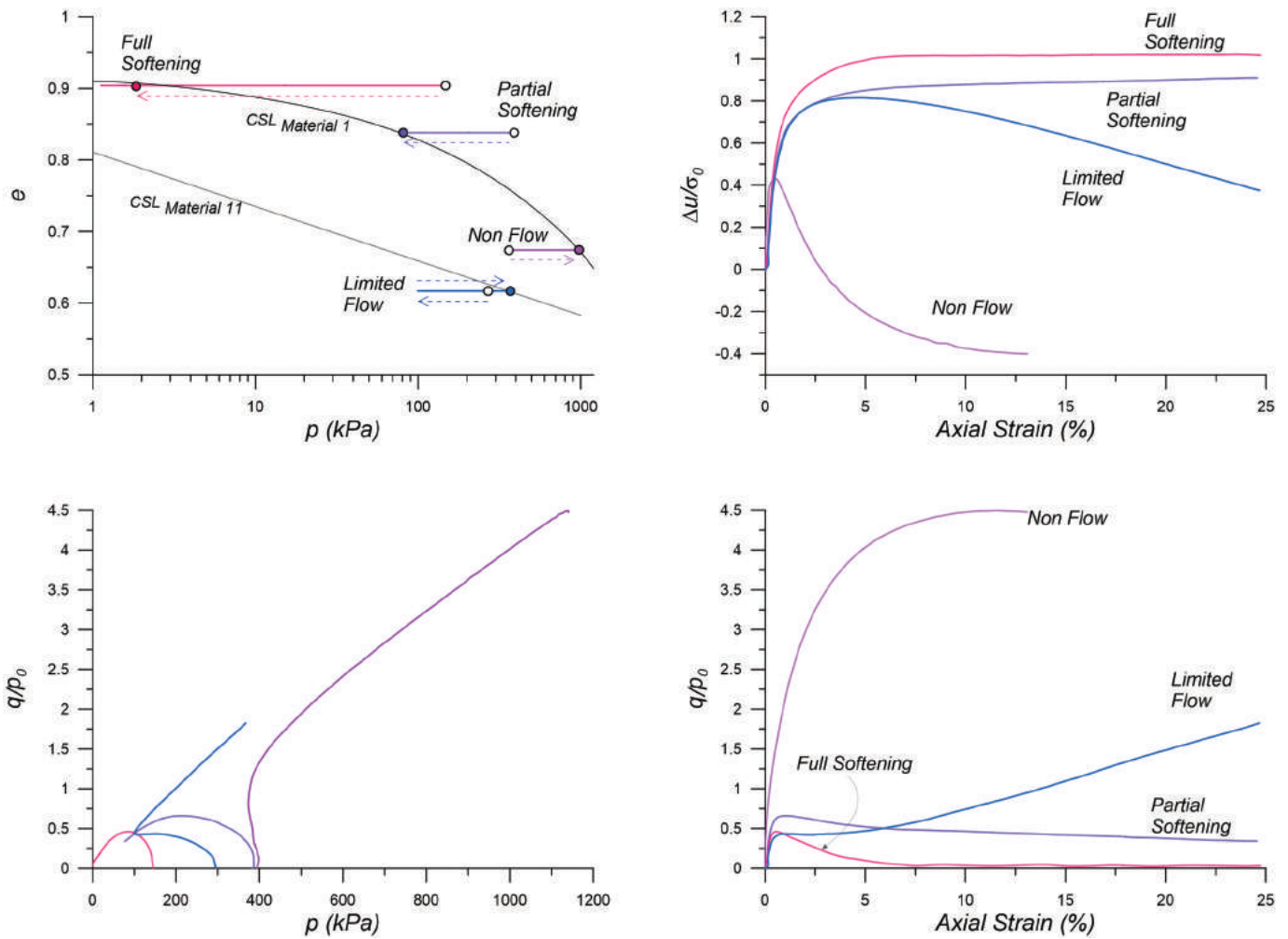
Reid and Fanni (2020) compared the CSLs obtained from intact tailings block samples and specimens prepared using moist tamping, concluding that the intact block samples generally tended towards the CSL obtained from the moist tamped specimens. Reid and Fanni (2020) also pointed out that slurry-deposited samples tended towards but did not reach the CSLs from moist tamped specimens and intact block samples. Furthermore, the moist tamping technique has also been used in the recent forensic studies involving mine tailings after the Fundao and Cadia TSFs failures (Morgenstern et al. 2016; Morgenstern et al. 2019). Figure 2 illustrates normalized stress–strain curves and stress paths obtained from drained and undrained triaxial for materials 01 to 03.

Data processing

The available laboratory tests for each material have been processed in a uniform manner. The following properties were evaluated for each material: (1) the critical state line (CSL), in the case of a linear CSL, the slope (λ_e), and the altitude at 1 kPa (Γ) are estimated using eq. 1a; in the case of a curve CSL, the parameters a, b, and c are estimated according to eq. 1b; (2) the stress ratio at critical state (M_{tc}), and the volumetric coupling (N), according to eq. 2a; (3) the state-dilatancy parameter (χ), according to eq. 2b; and (4) the stiffness–confinement dependence parameters (A, B) according to eqs. 3a to 3c.

M_{tc} was estimated as the slope of the line that joins the ultimate points in p (mean stress) versus q (deviatoric) plots or using eq. 2a, which is based on the strength–dilatancy relationship used in Jefferies and Been (2015). In eq. 2a, D_{min} represents the maximum dilatancy, and η_{max} is the maximum stress ratio. D_{min} was selected by plotting D versus the state parameter (ψ), after getting rid of potential fluctuations (noise) using a loess nonparametric fitting. η_{max} was selected from a η versus axial strain plot. N was also calculated from eq. 2a, using the slope of the η_{max} versus D_{min} relationship. χ was calculated from a plot of D_{min} versus ψ, according to eq. 2b. Finally, the parameters A and B were calculated by nonlinear regressions of the shear modulus (G) measured in the bender element tests versus the mean effective stress p according to eqs. 3a to 3c, using the two different functional forms. Equations 3b and 3c represent the functional form proposed by Hardin and Richart (1963) and Pestana and Whittle (1995), respectively.
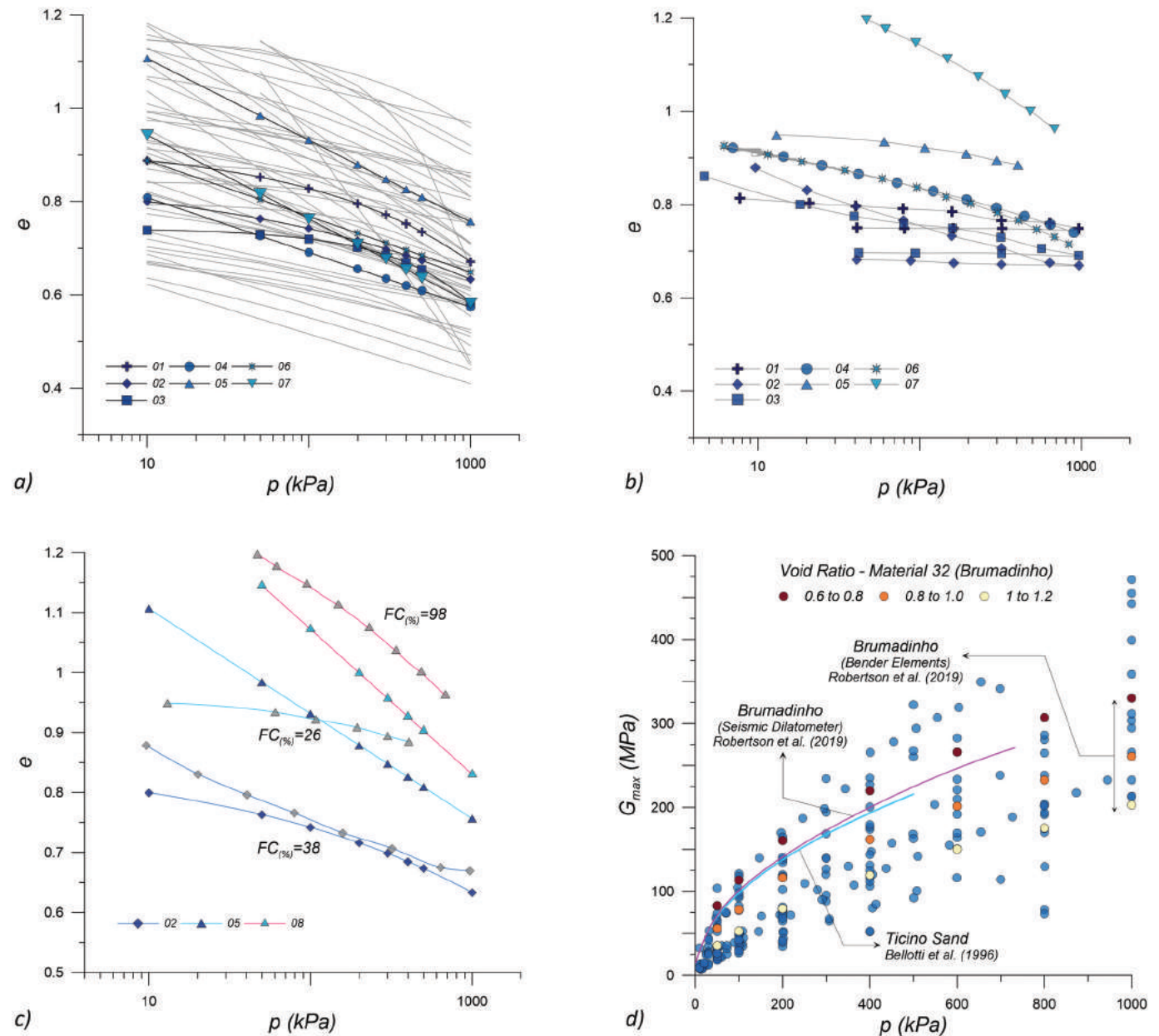
$$(1a) \quad e_{cs} = \Gamma - \lambda_e \ln p$$

$$(1b) \quad e_{cs} = a - b\left(\frac{p}{p_{atm}}\right)^c$$

$$(2a) \quad \eta_{max} = M_{tc} + (1 - D_{min})N$$

$$(2b) \quad D_{min} = \chi \psi$$

Fig. 5. (*a*) Distribution of CSLs for the materials considered in this study, (*b*) distribution of normally consolidation lines (NCL), (*c*) comparison of CSL and NCL for a subset of materials, (*d*) distribution of shear modulus (*G*) versus mean pressure (*p*) curves. [Colour online.]

$$(3a) \qquad G = AF(e)\left(\frac{p}{p_a}\right)^B$$

$$(3b) \qquad F(e) = \frac{(2.97 - e)^2}{(1 + e)}$$

$$(3c) \qquad F(e) = \frac{1 + e}{e}$$

It is important to highlight that Γ, λ_e, M_{tc}, N, χ, A, and B are often present as parameters in robust constitutive models, usually formulated for sands (although often named differently or represented by other proxies), and are the basis for the current mechanical-based understanding of static liquefaction. Figure 3 shows an example of the calculation of these parameters for

material 12. Figure 3*a* shows the estimation of the CSL, Fig. 3*b* shows the η_{max} versus D_{min} plot to estimate M_{tc} and N, Fig. 3*c* shows the state-dilatancy relationship to estimate χ, and Fig. 3*d* shows the *G* versus *p* plot to estimate *A* and *B*, according to eq. 3*a*.

In the case of undrained triaxial tests, we classified each test as (*i*) flow liquefaction with full softening, (*ii*) flow liquefaction with partial softening, (*iii*) limited flow liquefaction, and (*iv*) non-flow liquefaction. This classification is consistent with that in Rabbi et al. (2019). The subdivision of flow liquefaction cases in full softening and partial softening is also consistent with Soares and da Fonseca (2016). Figure 4 illustrates the adopted criteria using selected materials from our database.

The full softening corresponds to the cases that *p* and *q* reached values very close to zero, without any sign of a transformation point (i.e., a transition from contraction to dilation). The partial softening corresponds to cases that showed strain-softening after

Fig. 6. Variation of the CSL slope versus (*a*) FC and (*b*) PI. Variation of the CSL intercept at 1 kPa versus (*c*) FC and (*d*) LL × G_s. [Colour online.]
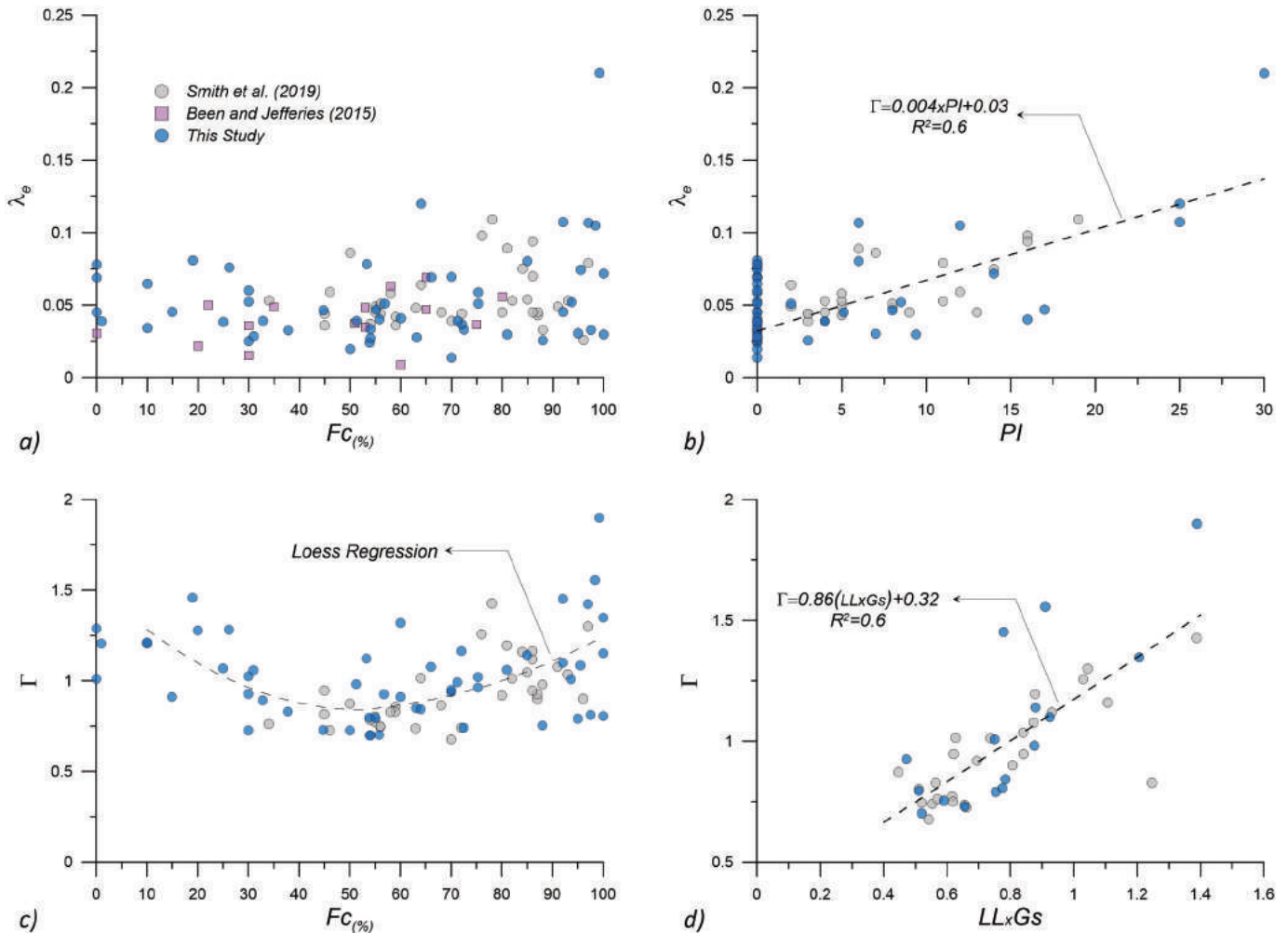
peak but with *q* values significantly larger than zero (we considered values 10 kPa as the threshold) by the end of the test. In addition, the following parameters were estimated for each test: the brittleness index $I_b = (Su_y - Su_r)/Su_y$ (Bishop 1971), where Su_y is the strength at peak (also called yield strength) and Su_r is the residual strength; the yield strength ratio (Su_y/σ'_0), where σ'_0 is the initial vertical effective stress; the residual strength ratio (Su_r/σ'_0); the excess pore pressure ratio ($r_u = \Delta u/\sigma'_0$, where Δu is the excess pore pressure); and the instability stress ratio η_{IL}, which corresponds to η at peak conditions in a *p* versus *q* plot when the behavior is associated with flow liquefaction. Of note, in the cases with limited flow (see Fig. 4), Su_r was selected as the minimum strength following strain-softening behavior, which corresponds to the so-called transformation point (Yoshimine and Ishihara 1998). This is consistent with Sadrekarimi (2014), who pointed out that when instability and deformation occur in field conditions, the soil behavior may become dynamic and turbulent due to inertial effects, and hardening may not be possible after the soil researches the transformation point under such circumstances.

We have also considered different definitions to quantify the state and its evolution; specifically, we considered the state parameter (ψ) defined by Been and Jefferies (1985), the state pressure index (I_p) defined by Wang et al. (2002), the modified state parameter (ψ_m) defined by Bobei et al. (2009), and a volumetric strain-based state parameter (ψ_v) defined in this study. Appendix B presents a detailed description of these parameters that

quantify the state of particulate materials (see eqs. B.1 to B.5 and Fig. B1 in Appendix B).

Trends in the mechanical response of mine tailings

Critical state parameters and stiffness

Figure 5*a* shows the distribution of the CSLs for all the materials considered in this study; it can be observed that the estimated CSLs were, in most cases, followed a linear relationship (in a semi-log space). In addition, the estimated CSLs cover a broad spectrum in the *e* versus *p* plane (the maximum difference in *e* for a given *p* is in the order of 0.55). Appendix Table A1 shows the estimated parameters for the CSLs. Figure 5*b* shows the distribution of the normally consolidation lines (NCL) for selected cases. Again, the NCLs cover a broad spectrum in the *e* versus *p* plane, with a maximum difference for e in the order of 0.6 for a given *p*. Figure 5*c* shows a comparison of CSLs and NCLs for three cases with different fines content. Interestingly, the finer the materials, the more the NCL and the CSL tend to be parallel, which affects the initial tailings state and then the mechanical response. Interested readers can also refer to Olson and Stark (2003) for additional discussions on the CSL and NCL relative location. Figure 5*d* illustrates the spectrum of the maximum shear modulus (*G*) variation (i.e., *G* versus mean pressure) estimated through bender element tests considering a broad range of densities.

Fig. 7. (*a*) Distribution of M_{tc} values for tailing and sand materials, (*b*, *c*) distribution of the *A* and *B* parameters in eqs. 3*a* and 3*b*, respectively, and (*d*) *A* versus state parameter variation. [Colour online.]
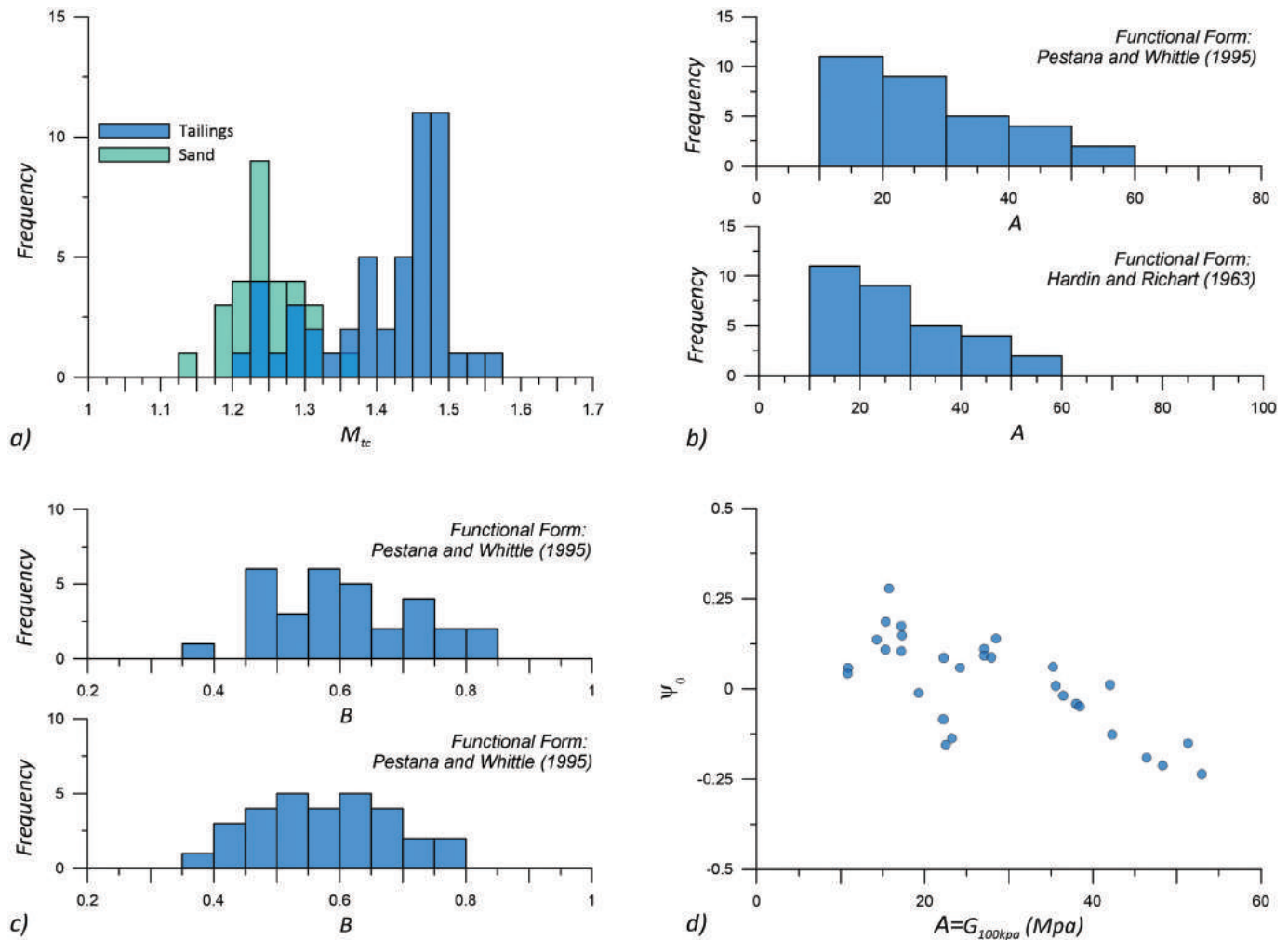
For illustrative purposes, we highlight how the initial void ratio influences *G* for material 32 (e.g., a lower initial void ratio produces a larger *G*). Note also that the order of magnitude for *G* in mine tailings can be somewhat comparable to the *G* values in natural sand in some cases (e.g., see the trend for Ticino sand that is included for reference). Hence, mine tailings, depending on their state (i.e., loose versus dense), may have a stiffness that is comparable to that of sand materials.

Figure 6 shows the variation of parameters that define the CSLs versus soil index parameters such as fines content (FC), plasticity index (PI), and liquid limit (LL). In these figures (Figs. 6*a* to 6*d*), we have also added the mine tailings data from Smith et al. (2019). Figure 6*a* shows the variation λ_e versus FC and Fig. 6*b* shows the variation of the λ_e versus PI. It can be seen that PI is correlated with λ_e ($R^2 = 0.6$ with a better correlation compared to FC) when a material presents a PI. This is expected because both PI and λ_e can be considered as proxies to compressibility.

The apparent correlation between PI and λ_e is also consistent with CSSM-based concepts (e.g., see Chapter 6 in Schofield and Wroth 1968). Hence, this suggests that the common approach of using FC for accounting for compressibility, as it is often done in the cyclic liquefaction assessments for sand materials with fines, may be questionable. PI, on the other hand, is related to the material's mineralogy, which is more fundamentally related to compressibility. This is consistent with the findings from Bray and

Sancio (2006), who evaluated the liquefaction triggering of fine-grained soils finding that PI is a better descriptor than FC. Figure 6*c* shows the variation of Γ (i.e., the altitude of the CSL at 1 kPa for the materials with a linear CSL) versus FC, and Fig. 6*d* shows the variation of Γ versus LL×G_s.

Figure 6*c* does not show a strong correlation between Γ and FC, but suggests that Γ tends to decrease with an initial increment of FC, a tendency that is reverted if FC keeps increasing further (note the Loess-based fitting line that illustrates this trend), which is consistent with the findings by previous studies that considered silty sands and sandy silts (e.g., Thevanayagam et al. 2002). Figure 6*d* evidences a stronger correlation between Γ and LL. This can be explained as LL being a measure of the water content of soil at an approximate strength of 2 kPa (Wood 1991). Considering that shear strength can be normalized, *p* will be low (for example, if the normalized strength is 0.2, *p* will be 10 to provide a strength of 2 kPa). The corresponding void ratio can be approximated as the water content (which is represented by LL) times G_s (assuming saturation); hence, by using a semi-logarithmic relationship for the CSL, a linear trend between Γ and LLG_s is expected (as illustrated in Fig. 6*d*), which is consistent with the findings in Smith et al. (2019). This is also consistent with CSSM concepts, which show a linear correlation between Γ and LL (e.g., see Chapter 6 in Schofield and Wroth 1968).

Fig. 8. (a) Variation of α and C_u. (b) Variation of β and C_u. The sand data was obtained from Cho et al. (2006). [Colour online.]
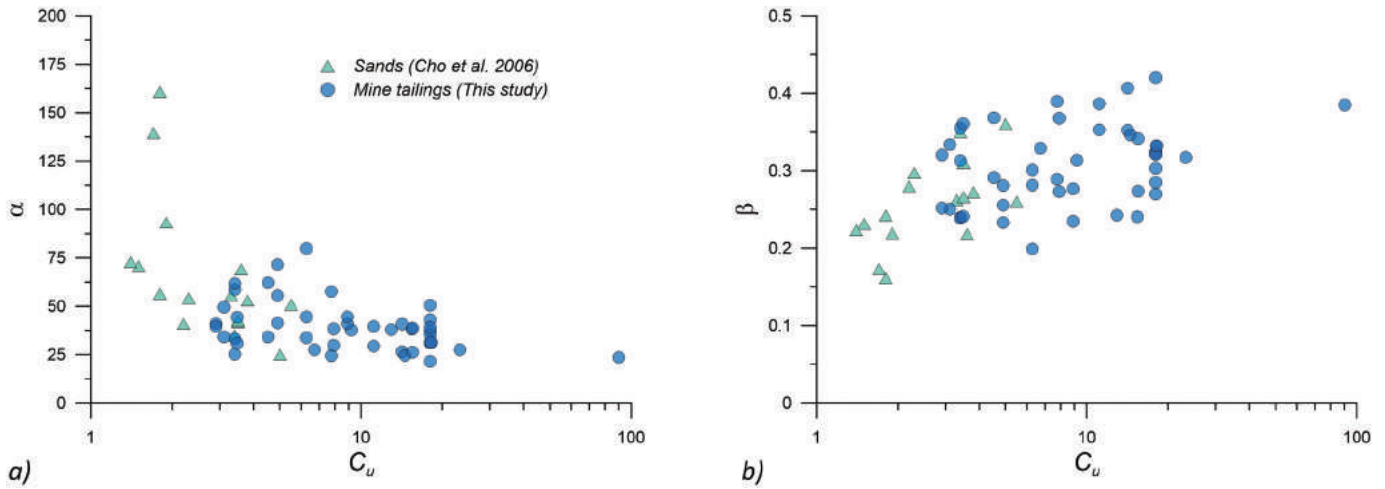

Fig. 9. Variation of Su_r/σ'_0 and Su_y/σ'_0 versus the brittleness index (panels (a) and (b), respectively); and Su_r/σ'_0 and Su_y/σ'_0 versus the initial state parameter (ψ_0) (panels (c) and (d), respectively). [Colour online.]
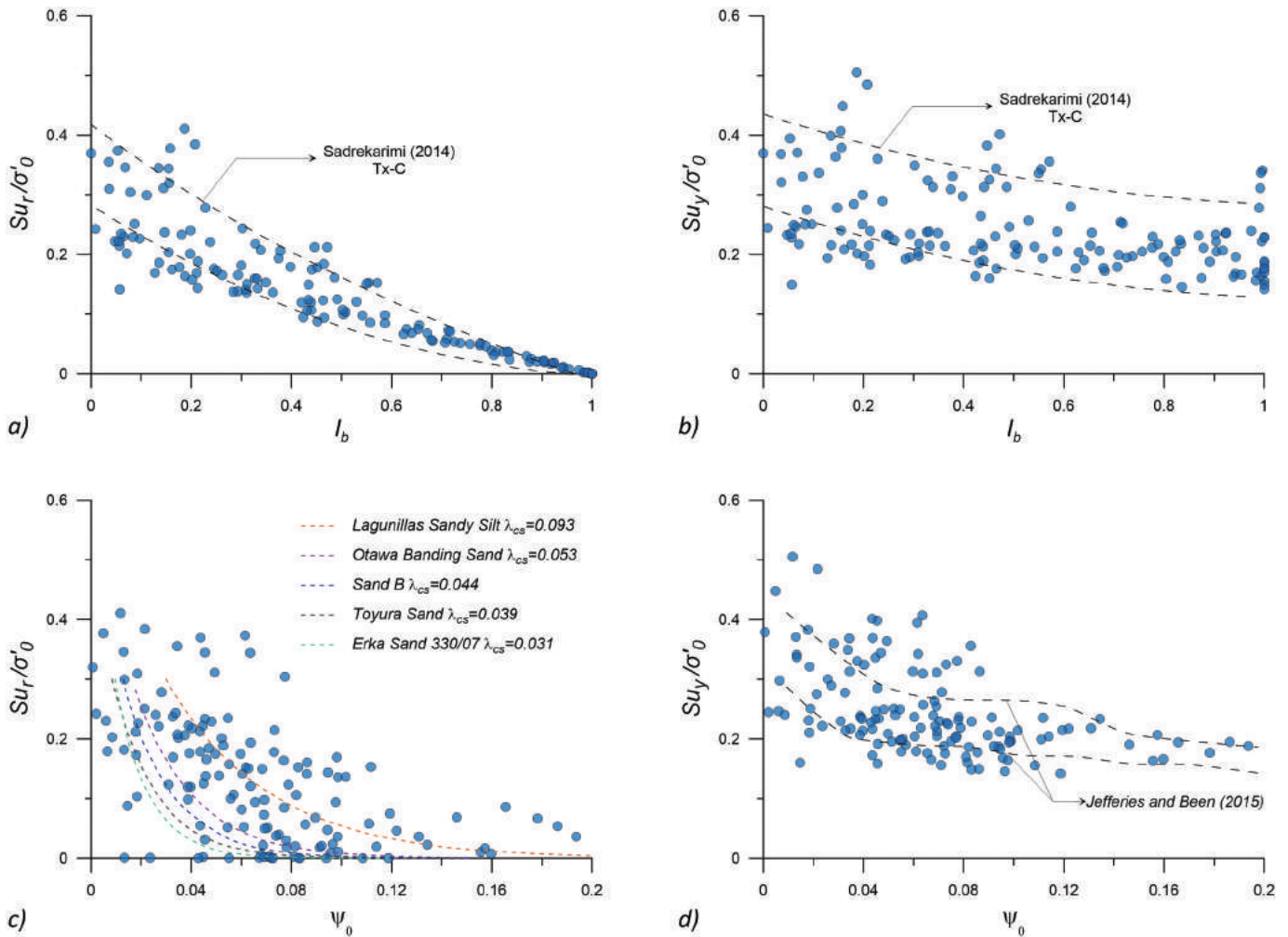
Figure 7a shows a histogram of M_{tc} values for tailings and sand materials. The M_{tc} values for sands were obtained from Jefferies and Been (2015). It can be observed that M_{tc} values for mine tailings are generally larger compared to sands, which has also been

observed in previous studies (e.g., Reid 2015). This is due to the angularity associated with mine tailings as a product of the mineral processing. Figures 7b and 7c show histograms for the A and B coefficients in eqs. 3a to 3c. It can be observed that the A coefficient

Fig. 10. Variation of Su_r/σ'_0 and Su_y/σ'_0 versus ψ_0/λ_e (panels (*a*) and (*b*), respectively); and $Su_r/(M_{tc}\sigma'_0)$ and $Su_y/(M_{tc}\sigma'_0)$ versus ψ_0/λ_e (panels (*c*) and (*d*), respectively). [Colour online.]
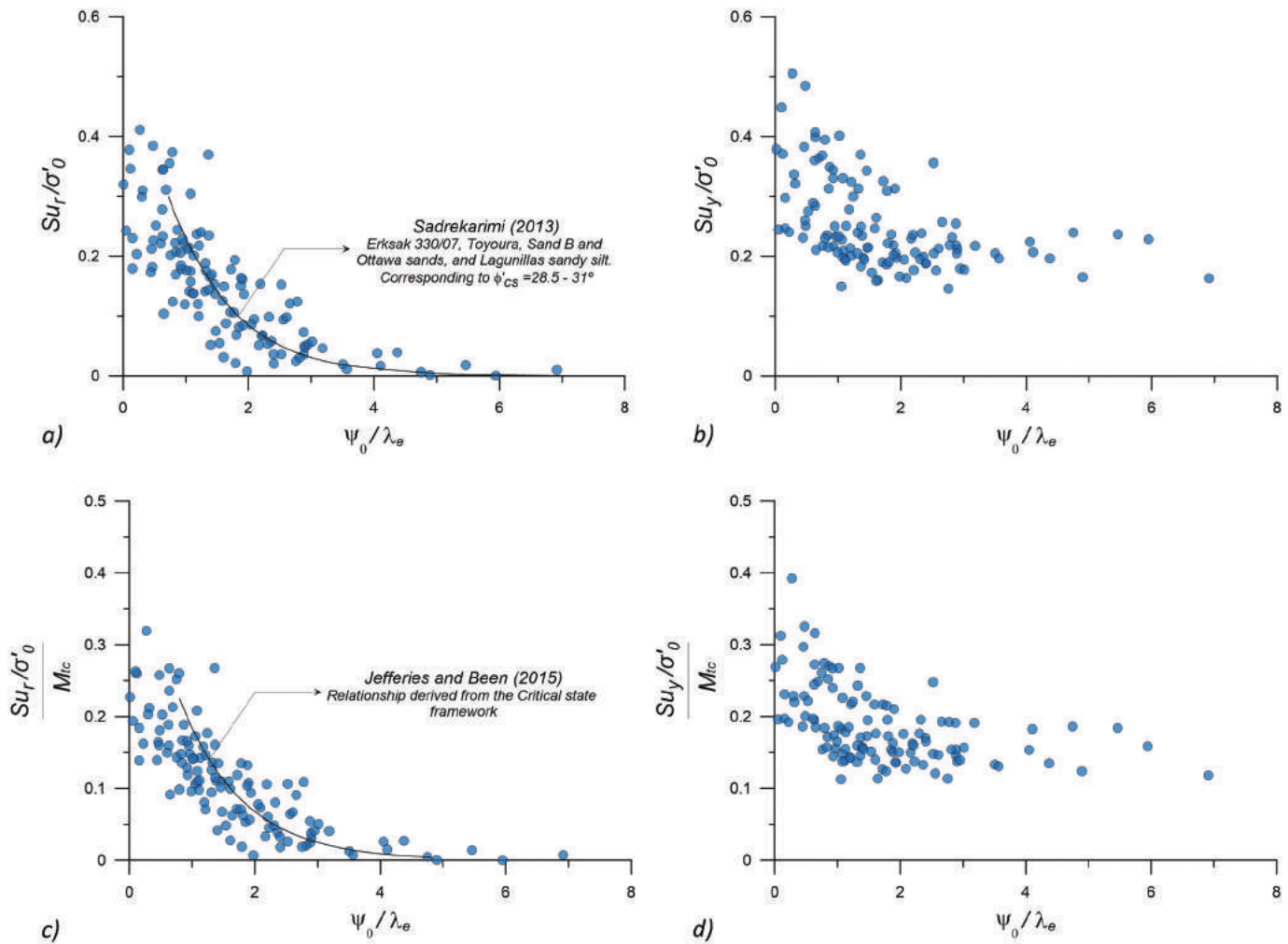
typically varies from 10 to 60 MPa, whereas the variation of *B* is generally between 0.4 and 0.7. To better understand the variation of the *A* coefficient, we plotted *A* versus the initial state parameter in Fig. 7*d*, which suggested a good correlation. Hence, larger *A* values are generally associated with dense materials (more negative state parameters), and lower *A* values are generally associated with loose materials (more positive state parameters). Furthermore, parameters *A* and *B* have shown to be dependent on particle shape and grain size distribution in sands (Cho et al. 2006; Payan et al. 2016). Parameter *A*, in particular, represents a volumetric-blended measure of soil particle stiffness. We explored the stiffness dependence on the particle size distribution of mine tailings using the α and β parameters ($V_s = \alpha\left(\dfrac{p}{1\,\text{kPa}}\right)^\beta$, where V_s is the shear wave velocity in m/s from bender tests). α and β are shear wave velocity counterparts of *A* and *B* and are used to integrate the sand data from Cho et al. (2006). Figure 8 shows the variation of C_u versus α and β, considering the data from this study and the data from Cho et al. (2006) for clean sands (which have a C_u lower than 5). The trends indicate that as C_u increases, α decreases and β increases; this finding is consistent with the observations of Payan et al. (2016) for clean sands and suggest that the overall effect of the irregularities introduced by different particle sizes is to hinder particle mobility and their ability to attain dense packing configurations leading to lower V_s (lower α) that are more susceptible to changes in stresses (higher β). Interestingly, it

can also be observed that the trends in mine tailings are consistent with the trends for sands.

Residual and peak strength

In Figs. 9 to 11 and figures in Appendix C, we discuss trends in terms of peak and residual shear strengths. Figures 9*a* and 9*b* shows the variations of Su_r/σ'_0 and Su_y/σ'_0 in terms of I_b, along with upper and lower bound trends for sand materials extracted from Sadrekarimi (2014). It is noticed that, in general, the trends are reasonably consistent.

Figure 9*c* shows the variation of Su_r/σ'_0 in terms of ψ_0 along with similar trends for sands with different compressibility (including the Lagunillas sandy silt) extracted from Sadrekarimi (2013). Figure 9*d* shows the variation of Su_y/σ'_0 in terms of and ψ_0 along with upper and lower bound trends for Su_y/σ'_0 in sands extracted from Jefferies and Been (2015). By examining Fig. 9*c*, the effect of compressibility is clearly observed (i.e., Su_r/σ'_0 in the case of sand materials increases with the increase of compressibility). In particular, the trends extracted for the Lagunillas sandy silt are more consistent with the overall variation of strength for mine tailings. The variation of Su_y/σ'_0 in Fig. 9*d* suggests that Su_y/σ'_0 tends to be larger in mine tailings compared to the sands in Jefferies and Been (2015) when ψ is lower than 0.1. To bring the effects of compressibility, we normalized the state parameter by λ_e. This normalization may also cancel out some fabric-related effects, as compressibility is expected to be influenced by fabric.

Fig. 11. (*a*) Su_y/σ'_0 dependence on the plastic modulus (H) and the rigidity index (I_r); (*b*) variation of Su_y/σ'_0 and $(d_{10,sand})/(d_{50,silt})$. [Colour online.]
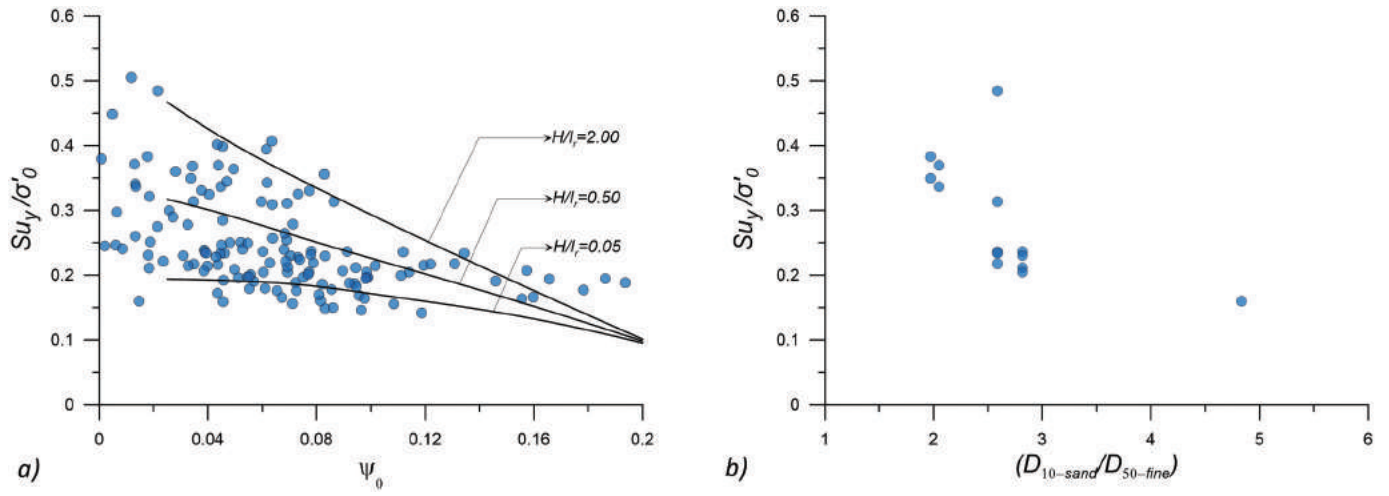

Fig. 12. Relationships between (*a*) I_b and ψ/λ_e, (*b*) I_b versus I_p, (*c*) ψ/λ_e versus I_p, and (*d*) ψ_m versus ψ/λ_e. [Colour online.]
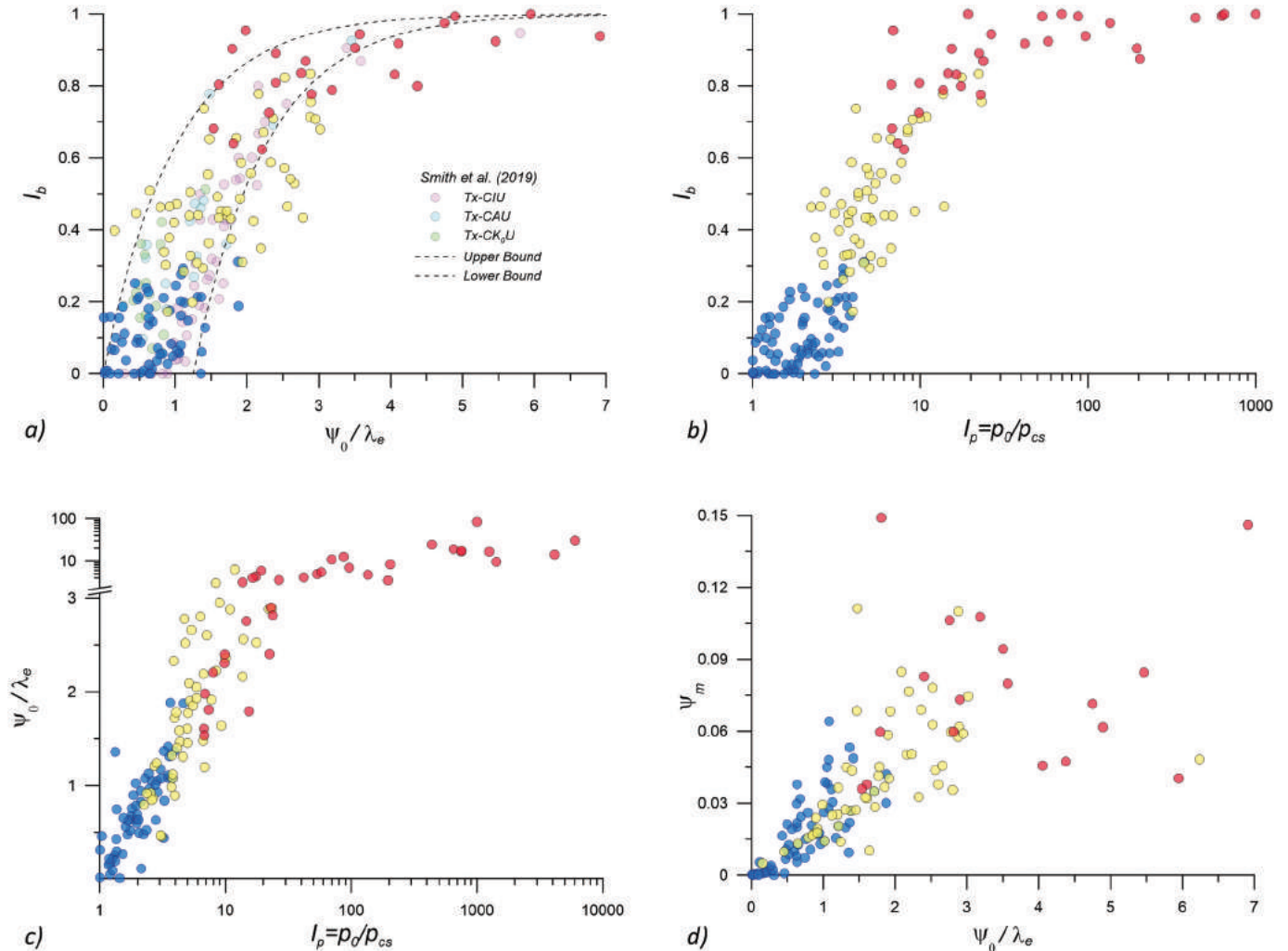
Fig. 13. Variation of the normalized instability stress ratio ($\eta_{\text{II}}/M_{\text{tc}}$) versus ψ/λ_e. [Colour online.]
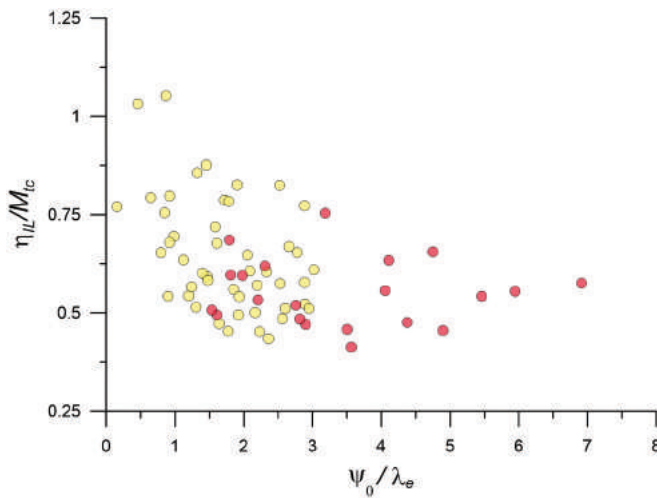
In cases where the CSL was a curve, we linearized the CSL in the range of stresses of interest and calculated a linearized λ_e. Figure 10a shows the variation of Su_r/σ_0' versus ψ/λ_e; now it can be observed that bringing λ_e decreases the variability in the trends, and the normalized trends for mine tailings are now more consistent with those for sand materials reported by Sadrekarimi (2013).

A similar effect can be observed in terms of Su_y/σ_0' in Fig. 10b, which shows that the normalization of the state parameter also helps to decrease the scatter. To account for the effects of angularity in strength, we further normalized the Su_r/σ_0' and Su_y/σ_0' ratios by M_{tc} and plotted the results in terms of ψ/λ_e. The results are shown in Figs. 10c and 10d. Recall that from CSSM concepts (e.g., Jefferies and Been 2015) $\text{Su}_r/(M_{\text{tc}}\sigma_0') = 0.5\exp(-\psi/\lambda_e)$, which is also plotted in Fig. 10c. This normalization brings an additional (minor) reduction to the scatter in the trends because compressibility and angularity effects are now considered through λ_e and M_{tc}. In addition, the experimental-based trends follow the trend of the aforementioned CSSM-based relationship. Appendix C shows the variation of the normalized peak and residual shear strength with respect to I_p, ψ_v/λ_e, and ψ_m/λ_e (Appendix C, Figs. C1–C3). In terms of I_p the scatter in the plots (Fig. C1) is comparable to the scatter in Figs. 10c and 10d because I_p brings state and compressibility information (recall that based on CSSM concepts $I_p = \exp(\psi_0/\lambda_e)$). In terms of ψ_v/λ_e, Fig. C2 shows that ψ_v helps to slightly reduce the scatter further with respect to ψ. This suggests that the volumetric strain potential brings relatively more information compared to the classical state parameter. In the case of ψ_m (Fig. C3), by using the pressure index on its formulation, it brings information on the strength and compressibility, making the trends similar to those in Figs. 10c and 10d.

Jefferies and Been (2015) suggest that Su_y is expected to depend on the ratio of the elastic modulus (e.g., G) and plastic moduli (H). Hence, Su_y is not only driven by frictional (M_{tc}) and compressibility properties, but also by G and H.

To further illustrate the influence of G and H on Su_y, we performed numerical simulations of undrained triaxial tests using the Norsand model considering different values for H/I_r (I_r is the rigidity index, defined as G/p) and the following Norsand parameters: $\lambda_e = 0.06$, $\Gamma = 1.1$, $M_{\text{tc}} = 1.40$, $N = 0.30$, $\chi = 4.0$, $\upsilon = 0.15$. These parameters are based on the average values observed in the mine tailings considered in this study. The results (normalized Su_y values) are shown in Fig. 11a, which suggest that H/I_r values of 0.05 and 2.0 are consistent with the lower and upper limits, respectively, for the observed Su_y values in our mine tailings database.

As a reference, Jefferies and Been (2015) found H/I_r values between 0.5 and 5 for sands. The H/I_r values in Fig. 11 can be used as upper and lower bounds to estimate H (given I_r) to better constrain the calibration of the Norsand model in numerical simulations that involve tailings materials.

Ni et al. (2004) suggested that the contribution of silt size particles to the strength of particulate materials with relatively low FC is related to the ratio of the void size distribution of the coarse fraction and the particle size distribution of the silt fraction, which they approximated by the ratio $(d_{10,\text{sand}})/(d_{50,\text{silt}})$, where $d_{10,\text{sand}}$ is the largest particle size in the smallest 10% of sand particles and $d_{50,\text{silt}}$ is the mean size of fine particles. They found that the contribution of the silt size to the strength decreases as $(d_{10,\text{sand}})/(d_{50,\text{silt}})$ increases. We explored the variation of this ratio against the strength data for the mine tailings in our database that have a FC lower than 40%. The results are presented in Fig. 11b and suggest that the strength decreases with the increase of $(d_{10,\text{sand}})/(d_{50,\text{silt}})$, which is consistent with Ni et al. (2004). However, in our database, we have only one material that shows a large $(d_{10,\text{sand}})/(d_{50,\text{silt}})$ ratio; hence, this trend should be further examined in future studies, and it is currently speculative.

### State and brittleness soil indexes

Figures 12a to 12d show the relationship between different parameters to represent the state and brittleness of a soil material. In these figures, the flow liquefaction cases that correspond to full softening and partial softening are presented in red and yellow colors, respectively. Figure 12a shows the relationship between I_b and ψ/λ_e, along with the data from Smith et al. (2019) and the upper and lower bounds proposed by them for contractive materials (i.e., $\psi > 0$). It can be observed that our data points are fairly consistent with these upper and lower bounds. The upper bound in this figure is representative of tests in anisotropic conditions and the lower bound with test with tests under isotropic conditions. Of note, the trends suggest that flow liquefaction cases with partial softening may have in general a I_b larger than 0.25 and a ψ/λ_e larger than 0.75, whereas the flow liquefaction cases with full softening may be associated with I_b values higher than 0.6 and ψ/λ_e values larger than 1.5. Figure 12b shows the relationship between I_b and I_p. As expected, I_p increases with an increase of I_b, and I_p values higher than 2.5 seem to be indicative of flow liquefaction with partial softening, whereas values larger than 10 may be indicative of potential flow liquefaction with full softening. Figure 12c shows the variation of ψ/λ_e and I_p, suggesting a good correlation between these parameters until flow liquefaction with full softening occurs in cases with $\psi/\lambda_e > 3$. Finally, Fig. 12d shows the variation of ψ_m and ψ/λ_e; again a good correlation is observed until $\psi/\lambda_e > 3$. Interestingly, ψ_m alone brings comparable information as ψ/λ_e because it also includes information on the state pressure index.

Instability stress ratio

Figure 13 shows the variation of the normalized instability stress ratio ($\eta_{\text{II}}/M_{\text{tc}}$) and the normalized state parameter (ψ_0/λ_e), for the cases where partial or full softening (i.e., flow liquefaction) was observed in undrained triaxial tests. As expected, $\eta_{\text{II}}/M_{\text{tc}}$ tends to decrease with the increase of increase of ψ_0/λ_e. In addition, we observe $\eta_{\text{II}}/M_{\text{tc}}$ values that are generally in the range of 0.6 to 1 for flow liquefaction cases with partial softening and values lower than 0.6 for flow liquefaction cases with full softening.

Excess pore pressures

Figure 14a shows the variation of $r_u = \Delta u/\sigma_0'$ versus I_b along with the trend of r_u relationships for sands considering triaxial extension (Tx-E), plane strain compression (PSC), and triaxial compression (Tx-C) conditions. The Tx-E and PSC trends were extracted from Sadrekarimi (2016), and the Tx-C trends were extracted from Sadrekarimi (2020).

Fig. 14. Variation of r_u versus (a) the brittleness index and (b) state parameter. [Colour online.]
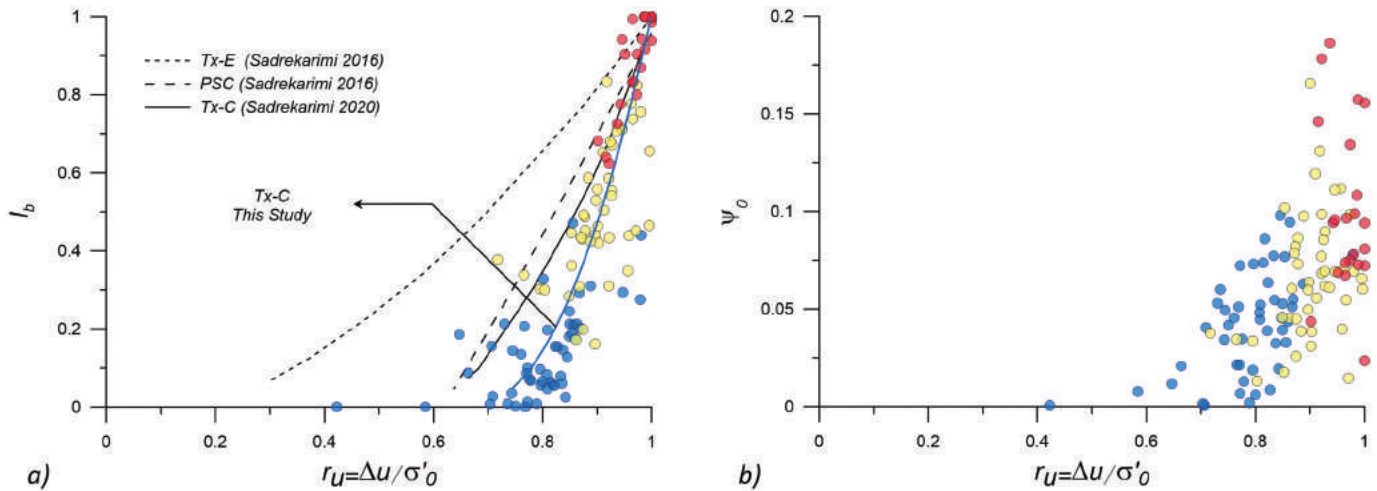
In general, it can be observed that flow liquefaction cases (partial and full softening) show r_u values large than 0.8, and the data are generally consistent with the average trend extracted for sand materials, but it is observed that the r_u values in mine tailings tend to be larger compared to sands in cases with partial softening. Figure 14b shows the r_u variation in terms of ψ. In general, large r_u values were observed with most values higher than 0.6 for $\psi > 0$. As expected, r_u increases with the increase in I_b and ψ, and an I_b higher than 0.1 or a ψ higher than 0 are indicative or large excess pore pressure generation (i.e., $r_u > 0.6$).

Dilatancy

Figure 15a shows the variation of the maximum dilatancy in triaxial CD tests versus the initial state parameter (ψ), considering the mine tailings from this study and data available in Jefferies and Been (2015) for sand materials. If we fit the data to the relationship suggested by Been and Jefferies (1985), given by $D_{min} = \chi \psi$, we obtain representative χ values of 3.0 for sands and 4.0 for tailings. This suggests that mine tailings have an average stronger scaling of dilatancy compared with sands, given a similar state parameter. This can be explained considering that χ can be though as a kinematic parameter related to the potential of particulate materials to re-accommodate particles. Given the more angularity of mine tailings compared to sands, mine tailings seem to have, on average, a higher potential on re-accommodating particles. Figure 15b shows the variation of χ and C_u/D_{50} for mine tailings and some well-known sand materials (i.e., Erksak, Braster, Changi, Fraser, Nerlek, and Ticino sands). The data for sands were obtained from Jefferies and Been (2015). C_u/D_{50} has been also used to examine the dilatancy of natural silts in Venice (Cola and Simonini 2002). It can be observed that the χ values in sands vary in a narrow range between 3.5 and 5.0, which correspond to C_u and C_u/D_{50} values that are also in a narrow range (1 to 3 and 3 to 10, respectively). In addition, χ in sands tend to slightly decrease with the increase of D_{50}. For example, χ for the Fraser River sand ($D_{50} = 0.3$ mm) is 5, χ for the Erksak sand ($D_{50} = 0.33$ mm) is 4.2, and χ for the Ticino sand ($D_{50} = 0.53$ mm) is 3.5. This variation of χ and D_{50} in sands for a narrow range of C_u (1.5–3.0) is consistent with the findings in Amirpour Harehdasht et al. (2019). In the case of mine tailings, we observe that χ tends to decrease with the increase of C_u/D_{50}. This trend is consistent with observations from DEM simulations (Yan and Dong 2011) that show that dilatancy tends to decrease with the increase of C_u. We also noticed that the lowest χ values (lower than 1.4) correspond to materials with large FC (larger than 85%) and important clay size fractions. This observation is consistent with the findings from Cola and Simonini (2002), who observed a decrease in the dilatancy of

Venice soils when their FC and clay size content increased. The materials 26 and 31 (which correspond to the Cadia and Brumadinho failures, respectively) showed large χ values (5.8 and 7.2, respectively). These large values may be associated with the large angularity on these materials and bonding effects, as suggested by Robertson et al. (2019) based on inspections of scanning electron microscope (SEM) images from the Brumadinho tailings. An inspection of SEM images in the Cadia tailings suggested similar patterns as those highlighted by Robertson et al. (2019). The bonding effects are illustrated in Figs. 15c and 15d, which show SEM images for the Brumadinho tailings. The bonding effects on the strength and dilatancy of mine tailings deserves further investigation. Finally, we have examined the effects of particle shape (e.g., roundness and sphericity) for the tailings materials where particle shape information is available. Figures 15e and 15f show that χ tends to reduce as roundness (R) and sphericity (S) increase (i.e., angularity decreases), which is consistent with the concept that χ is related the potential of particulate materials to re-accommodate particles.

Discussion

The trends presented in this study for the normalized Su_y and Su_r (i.e., Figs. 9 and 10) have been evaluated for Tx-C conditions; hence, they do not reflect shearing mode effects, loading anisotropy, and the effects of intermediate stresses. Sadrekarimi (2014), using a large database of hollow cylinder, direct simple shear, Tx-C, and Tx-E tests on natural sands, highlighted that Tx-C tests produce on average larger strengths than hollow cylinder or direct simple shear tests, which in turn produce large strengths than Tx-E tests. Sadrekarimi (2016), using a similar database, highlighted the importance of loading anisotropy and intermediate stresses. In addition, Sadrekarimi (2014) pointed out that normalized Su_y estimates from Tx-C tests were consistent with normalized Su_y estimates by Olson (2001) and Muhammad (2012) for flow liquefaction case histories, whereas normalized Su_r estimates from hollow cylinder tests or direct simple shear tests were more consistent to those in case histories. Hence, future studies should consider exploring loading anisotropic and intermediate effects systematically, as the currently available datasets on mine tailings to explore these effects are particularly scarce. Importantly, these effects should be explored in the context of the recent TSF failures.

In this context, the parameters discussed in this study are particularly useful to guide the calibration of multiaxial constitutive models, which are typically first calibrated under triaxial conditions. Once calibrated, they can provide predictions for other loading modes and be used in boundary value problems. For example,

Fig. 15. (*a*) Variation of ψ and D_{min} for sands and mine tailings. (*b*) Variation of χ and C_u/D_{50} (*c* and *d*) SEM images for the Brumadinho tailings suggesting bonding effects (Robertson et al. 2019). (*e*) Variation of χ and roundness. (*f*) Variation of χ and sphericity. The data for sand materials was obtained from Jefferies and Been (2015). [Colour online.]
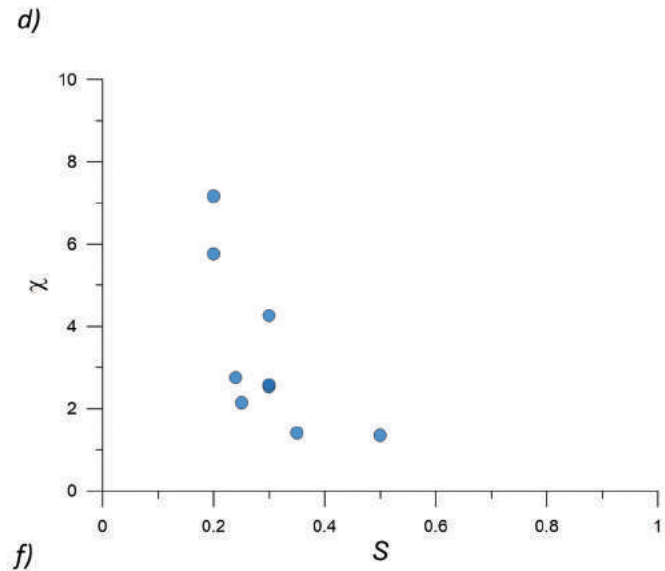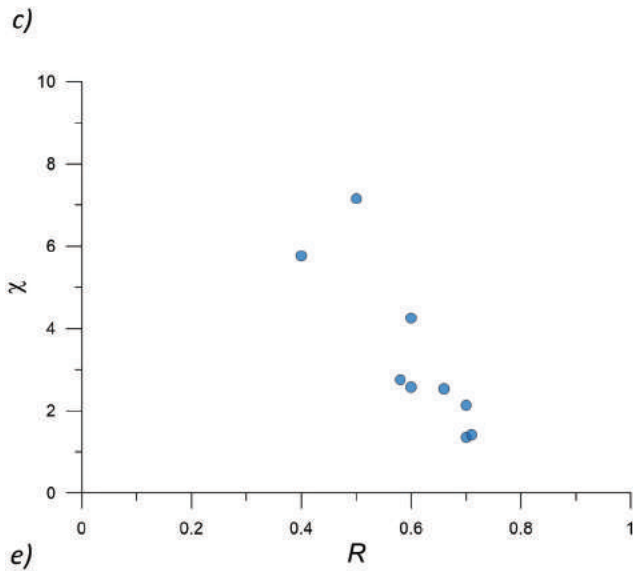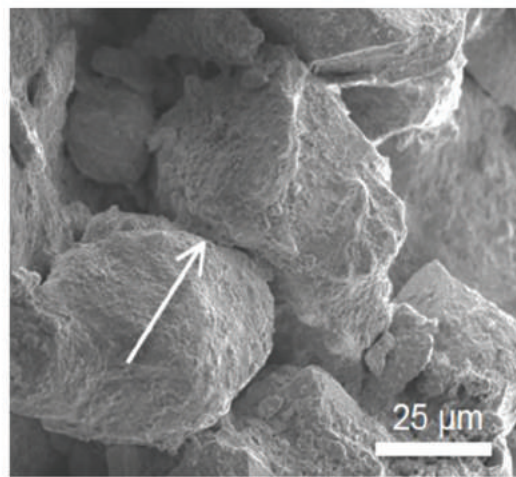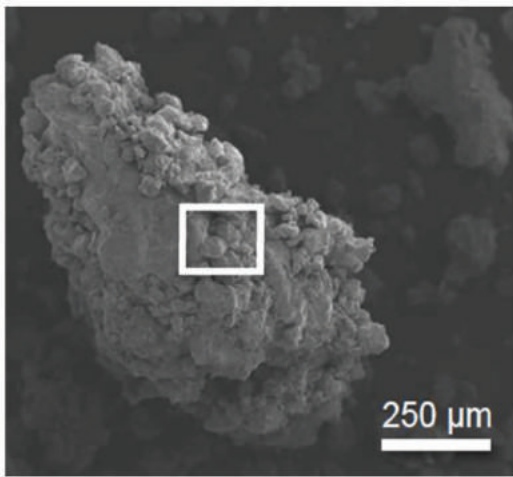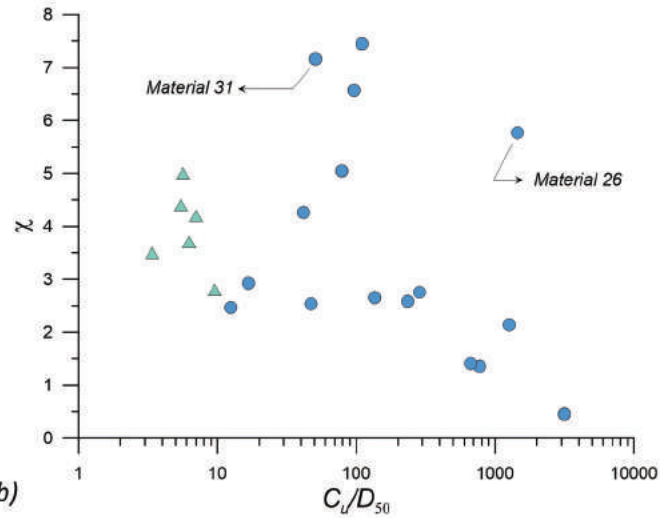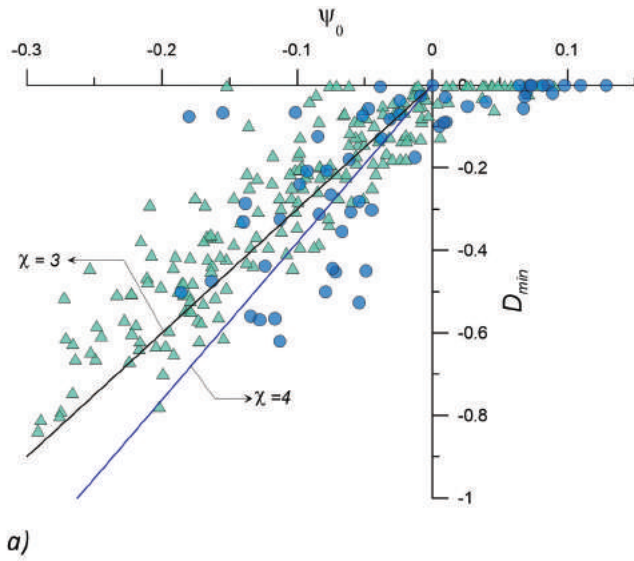
the calibration of the Norsand model (Jefferies 1993), which has been used in recent forensic studies, follows that philosophy. Moreover, the anisotropic critical state framework (Li and Dafalias 2012) and constitutive models developed under this framework (e.g., the Sanisand-F model developed by Petalas et al. 2020) can be used for introducing anisotropic loading anisotropy and intermediate stress effects after calibrations in the triaxial space. Of course, additional experimental data would greatly benefit the evaluation of the performance of these models in multiaxial conditions.

Finally, the experimental information used in this study is mainly composed of tests on moist tamped specimens, as they dominate the current state of practice in tailings engineering. For example, during the robin tests performed by Reid et al. (2021), more than 90% of the worldwide laboratories that participated used the moist tamping technique. It is recognized that moist tamping may not create the best representation of field conditions; however, it is used due to its advantages in CSSM-based engineering procedures (Jefferies and Been 2015; Reid and Fanni 2020; Reid et al. 2021; Schnaid 2013). Nevertheless, future studies should consider systematic investigations on the effects of reconstitution procedures on the mechanical response of mine tailings considering loading anisotropy and other effects. The work by Reid and Fanni (2020) comparing moist tamping and slurry deposition procedures against the response of intact block specimens is a step forward in that direction, but more research is warranted.

Conclusions

In this study, we have used critical state soil mechanics (CSSM) concepts to examined salient trends on the mechanical response of mine tailings in the context of static liquefaction, highlighting the role the relative proportions of different particles sizes and particle properties. The recent worldwide failures highlight the importance of an adequate understanding of the mechanical response of tailings materials. Tailings are geologically young materials, with angular grains rather than subrounded and often with lower proportions of quartz than many natural soils; thus, standard geotechnical correlations should not be taken as applicable to tailings without detailed consideration of these factors. Our results suggest that mine tailings fit the same framework as natural sands, with the key difference of showing a much larger M_{tc} and somewhat larger χ, both attributed to underlying particle shape, which then affects standard correlations. Thus, the mechanical response of mine tailings can be reasonably well explained once CSSM-based parameters such as Γ, λ_e, ψ, M_{tc}, χ, N, and G are incorporated.

We have observed that particle gradation influences the small strain shear stiffness and dilatancy, which is consistent with previous observations on sands. An increase in C_u typically reflects on a decrease in α and χ and an increase in β. The observed trends also suggest that particle shape affect dilatancy, χ tends to decrease as roundness and sphericity increase. In the case of mine tailings with large χ, bonding seems to have some effect, as suggested by Robertson et al. (2019). Bonding effects should be further explored in future research. Finally, the proportion of voids to the size of fine particles, represented through $(d_{10,sand})/(d_{50,silt})$, seems to influence shear strength of mine tailings with low FC, which has been also observed in natural soils; this is an aspect that should be also explored further in future studies.

Additional salient conclusions from this study include:

- The amount of FC is not a strong proxy to compressibility; hence, its use in liquefaction procedures to bring compressibility effects is questionable. In fine-grained plastic soils, PI seems to be a better proxy, since it is related to mineralogy. Bray and Sancio (2006) reached a similar conclusion when evaluating the liquefaction potential in fine-grained soils.

- The M_{tc} values in mine tailings (in the order of 1.4) are larger, on average, compared to M_{tc} values on natural sands (in the order of 1.2). This is associated with the particle shape of mine tailings, which tend to have more angular particles compared to the subrounded grains found in natural soils.

- Using the functional forms from Hardin and Richart (1963) and Pestana and Whittle (1995) for G (eq. 3), we observed that the parameter A that controls the magnitude of G correlates well with ψ_0. In addition, the parameter B that controls the dependence on p generally varies from 0.4 to 0.8.

- Compressibility can have an important effect on Su_r/σ'_0 and also controls Su_y/σ'_0. Hence, it should be carefully considered in evaluating appropriate Su_r/σ'_0 and Su_y/σ'_0 design values.

- In addition to M_{tc} and λ_e, the elastic and plastic moduli (G or I_r and H, respectively) control Su_y/σ'_0. We found that H/I_r values in the range of 0.05 to 2 represent the range of Su_y/σ'_0 values observed experimentally in our mine tailings database.

- In general, we observed that the state and brittleness indexes considered in this study such as ψ_0, ψ_m, ψ_v, I_p, and I_b are correlated.

- The normalized instability stress ratio (η_{II}/M_{tc}) for flow liquefaction cases with full softening was, in general, lower than 0.6.

- The trends suggest that flow liquefaction cases with partial softening may have in general I_b, ψ/λ, and I_p values larger than 0.25, 0.75, and 2.5, respectively, whereas flow liquefaction with full softening is associated with I_b, ψ/λ, and I_p values higher than 0.6, 1.5, and 10, respectively. We recommend using these values as part of preliminary screening procedures in engineering practice.

Data availability

Some or all data, models, or code generated or used during this study are available from the corresponding author by request. Specific items include the data used to generate the trends on the figures in this paper.

References

Al-Tarhouni, M., Simms, P., and Sivathayalan, S. 2011. Cyclic behaviour of reconstituted and desiccated-rewet thickened gold tailings in simple shear. Canadian Geotechnical Journal, 48 (7): 1044–1060. doi:10.1139/t11-022.

Amirpour Harehdasht, S., Hussien, M.N., Karray, M., Roubtsova, V., and Chekired, M. 2019. Influence of particle size and gradation on shear strength–dilation relation of granular materials. Canadian Geotechnical Journal, 56(2): 208–227. doi:10.1139/cgj-2017-0468.

Anderson, C., and Eldridge, T. 2011. Critical state liquefaction assessment of an upstream constructed tailings sand dam. Tailings and Mine Waste 2010. pp. 101–112. doi:10.1201/b10569-15.

Bedin, J., Schnaid, F., Da Fonseca, A.V., and Costa Filho, L.D.M. 2012. Gold tailings liquefaction under critical state soil mechanics. Géotechnique, 62(3): 263–267. doi:10.1680/geot.10.p.037.

Been, K., and Jefferies, M.G. 1985. A state parameter for sands. Géotechnique, 35(2): 99–112. doi:10.1680/geot.1985.35.2.99.

Been, K. 2016. Characterizing mine tailings for geotechnical design. In Geotechnical and Geophysical Site Characterisation 5, Australian Geomechanics Society, Sydney, Australia. pp. 41–56.

Bellotti, R., Jamiolkowski, M., Lo Presti, D.C.F., and O'Neill, D.A. 1996. Anisotropy of small strain stiffness in Ticino sand. Géotechnique, 46(1): 115–131. doi:10.1680/geot.1996.46.1.115.

Bishop, A.W. 1971. Shear strength parameters for undisturbed and remoulded soil specimens. Proceedings, Roscoe Memorial Symposium. Edited by R.H.G. Parry. Cambridge University Press, Cambridge, UK. pp. 3–58.

Bobei, D.C., Lo, S.R., Wanatowski, D., Gnanendran, C.T., and Rahman, M.M. 2009. Modified state parameter for characterizing static liquefaction of sand with fines. Canadian Geotechnical Journal, **46**(3): 281–295. doi:10.1139/T08-122.

Bray, J.D., and Sancio, R.B. 2006. Assessment of the liquefaction susceptibility of fine-grained soils. Journal of Geotechnical and Geoenvironmental Engineering, **132**(9): 1165–1177. doi:10.1061/(ASCE)1090-0241(2006)132:9(1165).

Carrera, A., Coop, M., and Lancellotta, R. 2011. Influence of grading on the mechanical behaviour of Stava tailings. Géotechnique, **61**(11): 935–946. doi:10.1680/geot.9.P.009.

Casagrande, A. 1936. Characteristics of cohesionless soils affecting the stability of earthfills. Journal of Boston Society of Civil Engineers, **23**: 257–276.

Chandler, R.J., and Tosatti, G. 1995. The Stava tailings dams failure, Italy, July 1985. Proceedings of the Institution of Civil Engineers, Geotechnical Engineering, **113**(2): 67–79. doi:10.1680/igeng.1995.27586.

Chen, H.W., and van Zyl, D.J.A. 1988. Shear strength and volume change behavior of copper tailings under saturated conditions. In Hydraulic fill structures. Edited by D.J.A. Van Zyl and S.G. Vick. pp. 430–451. ASCE, New York.

Cho, G.-C., Dodds, J., and Santamarina, J.C. 2006. Particle shape effects on packing density, stiffness, and strength: natural and crushed sands. Journal of Geotechnical and Geoenvironmental Engineering, **132**(5): 591–602. doi:10.1061/(ASCE)1090-0241(2006)132:5(591).

Cola, S., and Simonini, P. 2002. Mechanical behavior of silty soils of the Venice lagoon as a function of their grading characteristics. Canadian Geotechnical Journal, **39**(4): 879–893. doi:10.1139/t02-037.

Fourie, A.B., and Papageorgiou, G. 2001. Defining an appropriate steady state line for Merriespruit gold tailings. Canadian Geotechnical Journal, **38**(4): 695–706. doi:10.1139/t00-111.

Fourie, A.B., and Tshabalala, L. 2005. Initiation of static liquefaction and the role of K0 consolidation. Canadian Geotechnical Journal, **42**(3): 892–906. doi:10.1139/t05-026.

Gill, S.S. 2019. Geotechnical properties of tailings: effect of fines content. University of Toronto.

Hardin, B.O., and Richart, F.E. 1963. Elastic wave velocities in granular soils. Journal of the Soil Mechanics and Foundations Division, **89**: 33–65. doi:10.1061/JSFEAQ.0000493.

Hazen, A. 1918. A study of the slip in the Calaveras Dam. Engineering News Record, **81**: 1158–1164.

Jefferies, M.G. 1993. Nor-Sand: a simple critical state model for sand. Géotechnique, **43**(1): 91–103. doi:10.1680/geot.1993.43.1.91.

Jefferies, M.G., and Been, K. 2015. Soil liquefaction: a critical state approach. 2nd ed. CRC Press, Boca Raton, Fla., USA. doi:10.1201/b19114.

Ladd, R. 1978. Preparing test specimens using undercompaction. Geotechnical Testing Journal, **1**(1): 16–23. doi:10.1520/GTJ10364J.

Li, W. 2017. The mechanical behaviour of tailings. Ph.D. thesis, City University of Hong Kong, Hong Kong.

Li, W., and Coop, M.R. 2019. Mechanical behaviour of Panzhihua iron tailings. Canadian Geotechnical Journal, **56**(3): 420–435. doi:10.1139/cgj-2018-0032.

Li, W., Coop, M.R., Senetakis, K., and Schnaid, F. 2018. The mechanics of a silt-sized gold tailing. Engineering Geology, **241**: 97–108. doi:10.1016/j.enggeo.2018.05.014.

Li, X.S., and Dafalias, Y.F. 2012. Anisotropic critical state theory: role of fabric. Journal of Engineering Mechanics, **138**(3): 263–275. doi:10.1061/(ASCE)EM.1943-7889.0000324.

Lyman. 1938. Construction of Franklin Falls Dam. Report of US Army Corps of Engineers.

Macedo, J., and Petalas, A. 2019. Calibration of two plasticity models against the static and cyclic response of tailings materials. Proceedings of Tailings and Mine Waste, Vancouver, B.C.

Macedo, J., Bray, J., Olson, S., Bareither, C., and Arnold, C. 2020. TAILENG mine tailings database. Tailings and mine waste 2020 conference, Keystone, Colorado.

Morgenstern, N.R., Vick, S.G., and Zyl, D. 2015. Independent Expert Engineering Investigation and Review Panel. Report on Mount Polley Tailings Storage Facility Breach. British Columbia. Available from https://www.mountpolleyreviewpanel.ca/final-report.

Morgenstern, N.R., Vick, S.G., Viotti, C.B., and Watts, B.D. 2016. Fundao tailings dam review panel. Report in the immediate causes of the failure of the Fundao Dam. Cleary Gottlieb Steen and Hamilton LLP, New York. Available from http://fundaoinvestigation.com/the-panel-report/.

Morgenstern, N.R., Jefferies, M., Zyl, D., and Wates, J. 2019. Independent Technical Review Board. Report on NTSF Embankment Failure. Ashurst Australia. Available from https://www.newcrest.com/sites/default/files/2019-10/190417_Report%20on%20NTSF%20Embankment%20Failure%20at%20Cadia%20for%20Ashurst.pdf.

Muhammad, K. 2012. Case history-based analysis of liquefaction in sloping ground. Ph.D. thesis, University of Illinois at Urbana–Champaign, Urbana, Ill.

Ni, Q., Tan, T.S., Dasari, G.R., and Hight, D.W. 2004. Contribution of fines to the compressive strength of mixed soils. Géotechnique, **54**(9): 561–569. doi:10.1680/geot.2004.54.9.561.

Olson, S.M. 2001. Liquefaction analysis of level and sloping ground using field case histories and penetration resistance. Ph.D. thesis, University of Illinois at Urbana–Champaign, Urbana, Ill.

Olson, S.M., and Stark, T.D. 2003. Use of laboratory data to confirm yield and liquefied strength ratio concepts. Canadian Geotechnical Journal, **40**(6): 1164–1184. doi:10.1139/t03-058.

Payan, M., Khoshghalb, A., Senetakis, K., and Khalili, N. 2016. Effect of particle shape and validity of Gmax models for sand: A critical review and a new expression. Computers and Geotechnics, **72**: 28–41. doi:10.1016/j.compgeo.2015.11.003.

Pestana, J.M., and Whittle, A.J. 1995. Compression model for cohesionless soils. Géotechnique, **45**(4): 611–631. doi:10.1680/geot.1995.45.4.611.

Petalas, A.L., Dafalias, Y.F., and Papadimitriou, A.G. 2020. SANISAND-F: Sand constitutive model with evolving fabric anisotropy. International Journal of Solids and Structures, **188–189**: 12–31. doi:10.1016/j.ijsolstr.2019.09.005.

Rabbi, A.T.M.Z., Rahman, M.M., and Cameron, D.A. 2019. The relation between the state indices and the characteristic features of undrained behaviour of silty sand. Soils and Foundations, **59**(4): 801–813. doi:10.1016/j.sandf.2019.05.001.

Raposo, N. 2016. Deposição de rejeitados espessados. caraterização experimental e modelação numérica. PhD. Thesis, University of Porto.

Reid, D. 2015. Estimating slope of critical state line from cone penetration test — an update. Canadian Geotechnical Journal, **52**(1): 46–57. doi:10.1139/cgj-2014-0068.

Reid, D., and Fanni, R. 2020. A comparison of intact and reconstituted samples of a silt tailings. Géotechnique, 1–13. doi:10.1680/jgeot.20.p.020.

Reid, D., Fanni, R., Koh, K., and Orea, I. 2018. Characterisation of a subaqueously deposited silt iron ore tailings. Géotechnique Letters, **8**(4): 278–283. doi:10.1680/jgele.18.00105.

Reid, D., Fourie, A., Ayala, J.L., Dickinson, S., Ochoa-Cornejo, F., Fanni, R., et al. 2021. Results of a critical state line testing round robin programme. Géotechnique, **71**: 616–615. doi:10.1680/jgeot.19.P.373.

Riemer, M., Macedo, J., Roman, O., and Paihua, S. 2017. Effects of stress state on the cyclic response of mine tailings and its impact on expanding a tailings impoundment. In The 3rd International Conference on Performance-based Design in Earthquake Geotechnical Engineering, Vancouver.

Robertson, P.K., De Melo, L., Williams, D.J., and Wilson, G.W. 2019. Report of the Expert Panel on the Technical Causes of the Failure of Feijão Dam I. Available from http://www.b1technicalinvestigation.com/.

Sadrekarimi, A. 2013. Influence of state and compressibility on liquefied strength of sands. Canadian Geotechnical Journal, **50**(10): 1067–1076. doi:10.1139/cgj-2012-0395.

Sadrekarimi, A. 2014. Effect of the mode of shear on static liquefaction analysis. Journal of Geotechnical and Geoenvironmental Engineering, **140**(12): 04014069. doi:10.1061/(ASCE)GT.1943-5606.0001182.

Sadrekarimi, A. 2016. Static liquefaction analysis considering principal stress directions and anisotropy. Geotechnical and Geological Engineering, **34**(4): 1135–1154. doi:10.1007/s10706-016-0033-7.

Sadrekarimi, A. 2020. Forewarning of static liquefaction landslides. Journal of Geotechnical and Geoenvironmental Engineering, **146**(9): 04020090. doi:10.1061/(ASCE)GT.1943-5606.0002320.

Sadrekarimi, A., and Riveros, G.A. 2020. Static liquefaction analysis of the Fundão Dam failure. Geotechnical and Geological Engineering, **38**(6): 6431–6446. doi:10.1007/s10706-020-01446-8.

Schnaid, F., Bedin, J., Viana da Fonseca, A.J.P., and Costa Filho, L.D. 2013. Stiffness and strength governing the static liquefaction of tailings. Journal of Geotechnical and Geoenvironmental Engineering, **139**(12): 2136–2144. doi:10.1061/(ASCE)GT.1943-5606.0000924.

Schofield, A., and Wroth, C.P. 1968. Critical state soil mechanics. McGraw-Hill. ISBN:978-0641940484.

Shuttle, D., and Jefferies, M. 2016. Determining silt state from CPTu. Geotechnical Research, **3**(3): 90–118. doi:10.1680/jgere.16.00008.

Shuttle, D.A., and Cunning, J. 2007. Liquefaction potential of silts from CPTu. Canadian Geotechnical Journal, **44**(1): 1–19. doi:10.1139/t06-086.

Sladen, J.A., and Handford, G. 1987. A potential systematic error in laboratory testing of very loose sands. Canadian Geotechnical Journal, **24**(3): 462–466. doi:10.1139/t87-058.

Sladen, J.A., D'Hollander, R.D., and Krahn, J. 1985. The liquefaction of sands, a collapse surface approach. Canadian Geotechnical Journal, **22**(4): 564–578. doi:10.1139/t85-076.

Smith, K., Fanni, R., Capman, P., and Reid, D. 2019. Critical State testing of tailings: comparison between various tailings and implications for design. In Proceedings of Tailings and Mine Waste, Vancouver.

Soares, M., and da Fonseca, A.V. 2016. Factors affecting steady state locus in triaxial tests. Geotechnical Testing Journal, **39**(6): 20150228. doi:10.1520/GTJ20150228.

Thevanayagam, S., Shenthan, T., Mohan, S., and Liang, J. 2002. Undrained fragility of clean sands, silty sands, and sandy silts. Journal of Geotechnical and Geoenvironmental Engineering, **128**(10): 849–859. doi:10.1061/(ASCE)1090-0241(2002)128:10(849).

Torres, L.A. 2016. Use of the cone penetration test to assess the liquefaction potential of tailings storage facilities. Ph.D. thesis, University of the Witwatersrand, Johannesburg.

Torres-Cruz, L.A., and Santamarina, J.C. 2020. The critical state line of nonplastic tailings. Canadian Geotechnical Journal, **57**(10): 1508–1517. doi:10.1139/cgj-2019-0019.

USACE. 2016. National inventory of dams. US Army Corp of Engineers.

Wang, Z.-L., Dafalias, Y.F., Li, X.-S., and Makdisi, F.I. 2002. State pressure index for modeling sand behavior. Journal of Geotechnical and Geoenvironmental Engineering, **128**(6): 511–519. doi:10.1061/(ASCE)1090-0241(2002)128:6(511).

Wood, D.M. 1991. Soil behaviour and critical state soil mechanics. Cambridge University Press. doi:10.1017/CBO9781139878272.

Yan, W.M., and Dong, J. 2011. Effect of particle grading on the response of an idealized granular assemblage. International Journal of Geomechanics, **11**(4): 276–285. doi:10.1061/(ASCE)GM.1943-5622.0000085.

Yoshimine, M., and Ishihara, K. 1998. Flow potential of sand during liquefaction. Soils and Foundations, **38**(3): 189–198. doi:10.3208/sandf.38.3_189.

Appendix A

Table A1 presents the characteristic of the tailings materials considered in this study, such as the critical state line parameters (Γ, λ_e, or a, b, and c), the stress ratio at critical state (M_{tc}), liquid limit (LL), plasticity index (PI), fine contents (FC) and the specific gravity (G_s). In addition, we provide additional details for tests on materials 01 to 07. The details are summarized in Table A2, including the type of test (i.e., triaxial compression undrained (Tx-CU) and triaxial extension drained (Tx-CD)), the mean effective stress at consolidation (p_0) and critical state (p_{cs}), the shear stress at critical state (q_{cs}), the consolidated void ratio (e_0), and critical state void ratio (e_{cs}).

Table A1. Characteristics of tailings materials.

Material	Mineral	Γ / λ_e or a / b / c[b]	M_{tc}[c]	LL[d]	PI[d]	FC[d]	G_s[d]	Reference
1	Copper	0.924 / 0.096 / 0.421	1.49	—	0	15	3.12	This study
2	Copper	0.865 / 0.123 / 0.275	1.54	—	0	38	3.20	
3	Copper	0.742 / 0.022 / 0.856	1.49	—	0	73	3.20	
4	Copper	0.926 / 0.051	1.45	17	2	57	2.77	
5	Copper	1.281 / 0.076	1.50	—	0	26	2.80	
6	Copper	1.008 / 0.052	1.52	27	9	94	2.83	
7	Copper	1.123 / 0.078	1.47	—	0	53	2.80	
8	Copper	1.556 / 0.105	1.50	33	12	98	2.80	Riemer et al. 2017
9	Copper–zinc	1.14 / 0.08	1.40	26	6	85	3.38	Raposo 2016
10	Copper–zinc	1.423 / 0.107	1.36	35	6	97	3.38	
11	Copper	0.811 / 0.033	1.46	—	0	98	2.68	Macedo and Petalas 2019
12	Copper	0.79 / 0.03	1.46	28	7	95	2.69	
13	Copper	0.754 / 0.026	1.46	22	3	88	2.68	
14	Copper	0.989 / 0.124 / 0.7	1.31	52	22	99	2.67	Anderson and Eldridge 2011
15	Gold	0.953 / 0.104 / 0.414	1.33	—	0	70	3.00–3.15	Bedin et al. 2012; Schnaid et al. 2013
16	Gold	1.173 / 0.074 / 0.46	1.22	—	0	72	3.00–3.30	
17	Gold	0.958 / 0.128 / 0.594	1.24	—	0	70	3.00–3.15	
18	Bauxite	1.347 / 0.072	1.50	39	14	100	3.10	
19	Bauxite	1.122 / 0.13 / 0.381	1.29	31	5	92	3.00	
20	Zinc	1.076 / 0.069	1.20	—	0	72	3.61	Shuttle and Cunning 2007
21	Iron	0.799 / 0.087 / 0.445	1.41	20	0	20	3.37	Li and Coop 2019
22[a]	Iron	0.797 / 0.022 / 0.863	1.33	—	0	54	2.95	Morgenstern et al. 2016
23	Gold	1.226 / 0.334 / 0.188	1.41	—	0	96	2.89	Li et al. 2018
24[a]	Gold	0.729 / 0.046	1.50	24	8	56	2.73	Morgenstern et al. 2019
25[a]	Gold	0.85 / 0.028	1.50	—	0	63	2.63	
26[a]	Gold	0.736 / 0.04	1.50	19	16	56	2.74	
27[a]	Gold	0.795 / 0.047	1.50	19	17	55	2.69	
28	Iron	1.157 / 0.085	1.40	25	25	92	3.11	Li 2017
29	Iron	0.912 / 0.128 / 0.296	1.36	25	25	64	3.14	
30[a]	Iron	1.108 / 0.248 / 0.147	1.38	20	4	51	4.38	Robertson et al. 2019
31[a]	Iron	0.896 / 0.04 / 0.562	1.38	—	0	33	4.89	
32[a]	Iron	0.996 / 0.067 / 0.404	1.38	21	4	71	3.89	
33	Platinum	1.205 / 0.034	1.25	—	0	10	3.51	Torres 2016
34	Platinum	0.928 / 0.025	1.29	—	0	30	3.43	
35	Platinum	1.061 / 0.03	1.25	—	0	81	3.59	
36	—	1.284 / 0.069	1.46	—	0	0	2.93	Gill 2019
37	—	1.212 / 0.065	1.49	—	0	10	2.93	
38	—	1.024 / 0.052	1.57	—	0	30	2.93	
39	—	1.41 / 0.117	1.49	—	0	60	2.93	
40	—	1.152 / 0.053 / 0.967	1.43	—	0	100	2.94	
41	Iron	0.962 / 0.051	1.43	—	0	75	2.96	Reid and Fanni 2020
42	Iron	1.02 / 0.059	1.46	—	0	75	2.96	
43	Iron	0.925 / 0.045	1.47	—	0	0	2.78	Reid et al. 2018
44	Gold	0.732 / 0.113 / 0.275	1.45	—	0	54	2.78	Reid et al. 2021
45	Gold	0.741 / 0.132 / 0.242	1.46	—	0	54	2.78	
46	Gold	1.263 / 0.191 / 0.256	1.29	—	0	0	2.69	Fourie and Papageorgiou 2001
47	Gold	1.459 / 0.081	1.10	—	0	19	2.69	
48	Gold	1.057 / 0.028	1.14	—	0	31	2.69	
49	Gold	0.91 / 0.041	1.24	—	0	60	2.69	
50	Fluorite	1.016 / 0.078 / 0.545	1.44	—	0	0	2.72	Carrera et al. 2011
51	Fluorite	0.74 / 0.096 / 0.413	1.45	—	0	30	2.75	
52	Fluorite	1.053 / 0.45 / 0.069	1.44	—	0	50	2.77	
53	Fluorite	0.849 / 0.128 / 0.233	1.38	9.4	9.4	100	2.83	

[a]Materials 22, 24–27, and 30–32 correspond to the case histories of Fundao, Cadia, and Brumadinho, respectively.
[b]a, b, and c parameters are reported in cases where CSL fits a curve, while Γ and λ_e are reported for the conventional approach.
[c]M_{tc} is the critical state stress ratio.
[d]LL, PI, FC, and G_s represent the liquid limit, plasticity index, fine contents, and specific gravity, respectively.

Table A2. Additional information for tests on materials 1 to 7.

Material	Type of test	Test ID	p_0	e_0	p_{cs}	q_{cs}	e_{cs}
1	Tx-CU	M1-1	394	0.67	1140	1770	0.67
	Tx-CU	M1-2	400	0.71	762	1092	0.71
	Tx-CU	M1-3	142	0.90	0	5	0.90
	Tx-CU	M1-4	419	0.88	19	30	0.88
	Tx-CU	M1-5	423	0.68	896	1403	0.68
	Tx-CU	M1-6	402	0.84	78	130	0.84
	Tx-CU	M1-7	297	0.79	178	268	0.79
	Tx-CU	M1-8	203	0.93	0	9	0.93
	Tx-CD	M1-9	191	0.78	382	571	0.77
2	Tx-CU	M2-1	196	0.81	9	19	0.81
	Tx-CU	M2-2	386	0.75	70	63	0.75
	Tx-CU	M2-3	289	0.77	21	30	0.77
	Tx-CU	M2-4	398	0.63	1066	1643	0.63
	Tx-CU	M2-5	196	0.83	1	8	0.83
	Tx-CD	M2-6	143	0.71	292	446	0.71
	Tx-CD	M2-7	291	0.78	585	878	0.67
	Tx-CD	M2-8	288	0.80	593	907	0.69
	Tx-CU	M2-9	354	0.68	418	722	0.68
3	Tx-CU	M3-1	193	0.74	28	57	0.74
	Tx-CU	M3-2	361	0.73	59	79	0.73
	Tx-CU	M3-3	322	0.73	64	106	0.73
	Tx-CD	M3-4	343	0.74	701	1069	0.65
	Tx-CU	M3-5	419	0.71	119	183	0.71
	Tx-CU	M3-6	140	0.74	0	0	0.74
	Tx-CD	M3-7	295	0.70	572	831	0.65
	Tx-CU	M3-8	319	0.65	573	849	0.65
	Tx-CU	M3-9	381	0.65	311	520	0.65
4	Tx-CU	M4-1	41	0.84	7	11	0.84
	Tx-CU	M4-2	94	0.81	14	29	0.81
	Tx-CU	M4-3	193	0.70	49	63	0.70
	Tx-CD	M4-4	201	0.72	415	641	0.65
5	Tx-CU	M5-1	41	0.86	266	392	0.86
	Tx-CU	M5-2	90	0.84	325	477	0.84
	Tx-CU	M5-3	169	0.85	292	463	0.85
	Tx-CU	M5-4	395	0.73	737	1117	0.73
6	Tx-CU	M6-1	200	0.72	225	324	0.72
	Tx-CU	M6-2	80	0.75	97	140	0.75
	Tx-CD	M6-3	153	0.81	81	110	0.73
	Tx-CD	M6-4	42	0.89	73	102	0.82
7	Tx-CU	M7-1	394	0.68	234	353	0.68
	Tx-CD	M7-2	199	0.72	381	546	0.66
	Tx-CD	M7-3	49	0.80	88	122	0.76

Appendix B

This appendix presents the different state definitions used in this study. Figure B1 shows all the state definitions graphically.

State parameter

Been and Jefferies (1985) defined the state parameter as the difference between the current void ratio (e) and the void ratio at critical state (e_{cs}) for the same p. Equation B1 defines the state parameter. A ψ value higher than 0 is indicative of a contractive behavior (i.e., flow liquefaction), and a ψ value lesser than 0 is indicative of dilative behavior. However, case histories suggest that ψ higher than -0.05 is a better indicator of flow liquefaction (e.g., Shuttle and Cunning 2007).

$$(B1) \qquad \psi = e - e_{cs}$$

State pressure index

Wang et al. (2002) defined the state pressure index (I_p) as the ratio of the current mean effective pressure (p) and the mean

Fig. B1. Definition of the parameters considered in this study to characterize soil state. [Colour online.]
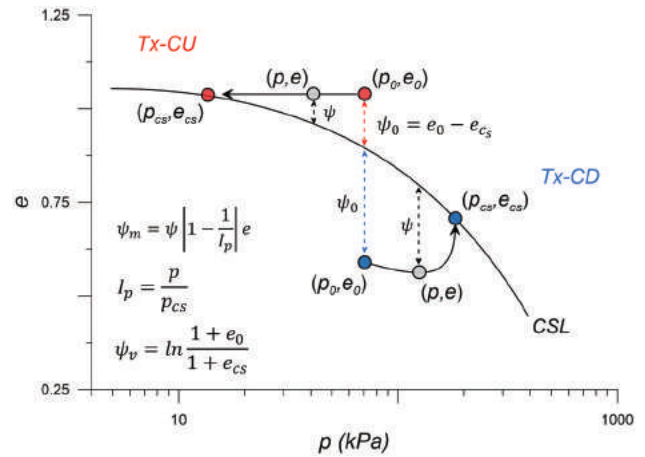
effective pressure at the critical state (p_{cs}) for the same void ratio. I_p is defined according to eq. B2:

$$(B2) \qquad I_p = \frac{p}{p_{cs}}$$

An I_p value higher than 1 is indicative of a contractive behavior, and an I_p value lesser than 1 is indicative of dilative behavior.

Modified state parameter

Bobei et al. (2009) combined ψ and I_p to define a modified state parameter ψ_m, which is calculated as

$$(B3) \qquad \psi_m = \psi \left| 1 - \frac{1}{I_p} \right| e$$

Bobei et al. (2009) argued that this modification would be particularly useful in the case of a curve CSL and found that ψ_m provided valuable insight for flow liquefaction cases. However, they found that ψ_m could be problematic for dilative materials because I_p may be much lesser than 1, causing a large increment in ψ_m.

Volumetric strain-based state parameter potential

We also considered a state definition based on the volumetric strain potential, which has been denoted as ψ_v. Considering the critical state theory axiom that all stress paths go to the critical state, for a constant p stress path, we will have that the volumetric strain can be estimated by

$$(B4) \qquad d\varepsilon_v = -\frac{dv}{v}$$

where $v = 1 + e$ corresponds to the specific volume.

Integrating eq. B4 from initial conditions to the critical state conditions, we will obtain

$$\varepsilon_v = \ln(v_0) - \ln(v_{cs})$$

where $v_0 = 1 + e_0$, $v_{cs} = 1 + e_{cs}$, e_0 is the initial void ratio, and e_{cs} is the critical void ratio. This leads to the definition of a volumetric strain-based state parameter as

$$(B5) \qquad \psi_v = \ln\left(\frac{1 + e_0}{1 + e_{cs}}\right)$$

Appendix C

Here we present the variation of Su_r/σ'_0 and Su_y/σ'_0 with respect to the additional state definitions considered in this study (i.e., I_p, ψ_v, and ψ_m).

Figures C1a and C1b show the variation of Su_r/σ'_0 and Su_y/σ'_0 versus the pressure index (I_p). Recall that based on CSSM concepts, the relation $p_{cs}/p = \exp(-\psi_0/\lambda_e)$ holds (e.g., Jefferies and Been 2015). The scatter in the plots is comparable to the scatter in Figs. 10c and 10d when λ_e and M_{tc} were used for the normalizations because I_p brings state and compressibility information. Figures C2a and C2b show the variation of $Su_r/(M_{tc}\sigma'_0)$ and $Su_y/(M_{tc}\sigma'_0)$ relative to ψ_v/λ_e. Figures C3a and C3b show the variation of $Su_r/(M_{tc}\sigma'_0)$ and $Su_y/(M_{tc}\sigma'_0)$ versus ψ_m/λ_e. In Fig. C2, it is observed that ψ_v helps to reduce the scatter further respect to ψ, whereas the scatter in Fig. C3 is comparable to that in Figs. 10c and 10d. This suggests that the volumetric strain potential brings relatively more information compared to the classical state parameter. In the case of the ψ_m, by using the pressure index on its formulation, it brings information on the strength and compressibility, making the trends similar to those in Figs. 10c and 10d.

Fig. C1. (a) Variation of Su_r/σ'_0 versus I_p; (b) variation of Su_y/σ'_0 versus I_p. [Colour online.]
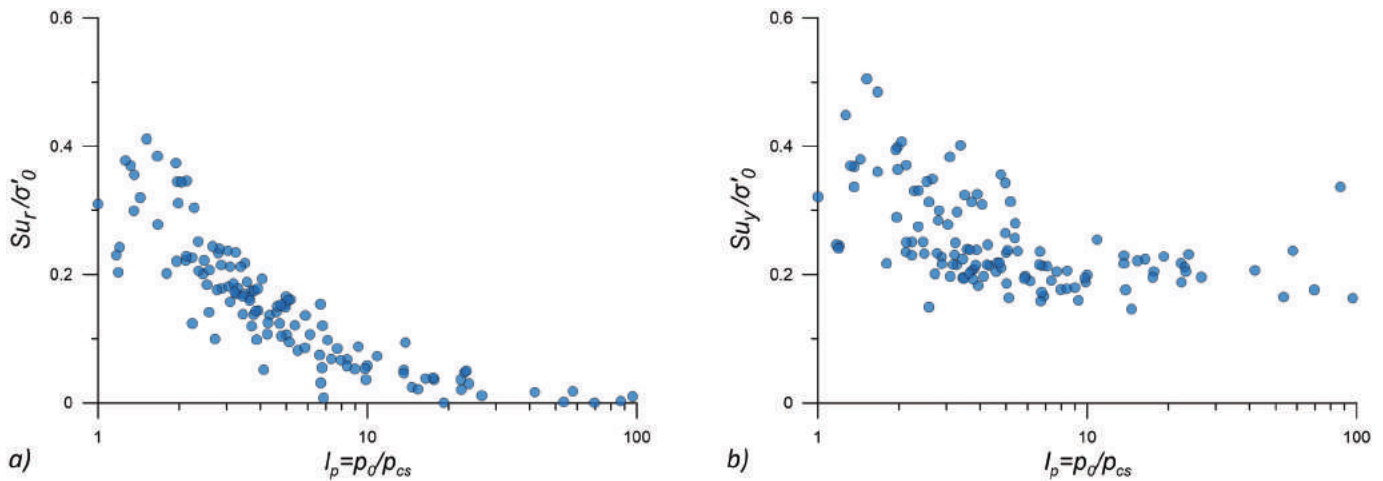
Fig. C2. (a) $Su_r/(M_{tc}\sigma'_0)$ versus ψ_v/λ_e; (b) $Su_y/(M_{tc}\sigma'_0)$ versus ψ_v/λ_e. [Colour online.]

Fig. C3. (a) $Su_r/(M_{tc}\sigma'_0)$ versus ψ_m/λ_e; (b) $Su_y/(M_{tc}\sigma'_0)$ versus ψ_m/λ_e. [Colour online.]